1 **Common Mechanism of SARS-CoV and SARS-CoV-2 Pathogenesis across Species**

2

3 Alexandra Schäfer[1*#], Lisa E. Gralinski[1*], Sarah R. Leist[1*], Emma S. Winkler[2,3], Brea K.

4 Hampton[4,5], Michael A. Mooney[6,7,8], Kara L. Jensen[1], Rachel L. Graham[1], Sudhakar

5 Agnihothram[1], Sophia Jeng[6,9], Steven Chamberlin[7,8], Timothy A. Bell[4], D. Trevor Scobey[1], Laura

6 A. VanBlargan[2], Larissa B. Thackray[2], Pablo Hock[4], Darla R. Miller[4,10], Ginger D. Shaw[4,10],

7 Fernando Pardo Manuel de Villena[4], Shannon K. McWeeney[6,7,8,9], Stephanie A. Montgomery[10,11],

8 Michael S. Diamond[2,3,12], Mark T. Heise[4,13,17], Vineet D. Menachery[14,15,16], Martin T. Ferris[4#],

9 Ralph S. Baric[1,13,17#]

10

11 [1]Department of Epidemiology, University of North Carolina at Chapel Hill, Chapel Hill, NC, USA

12 [2]Department of Medicine, Washington University School of Medicine, St. Louis, MO, USA

13 [3]Department of Pathology & Immunology, Washington University School of Medicine, St. Louis,

14 MO, USA

15 [4]Department of Genetics, University of North Carolina at Chapel Hill, Chapel Hill, NC, USA

16 [5]Curriculum in Genetics and Molecular Biology, University of North Carolina at Chapel Hill, Chapel

17 Hill, NC, USA

18 [6]Knight Cancer Institute, Oregon Health & Science University, Portland, OR, USA

19 [7]Division of Bioinformatics and Computational Biology, Oregon Health & Science University,

20 Portland, OR, USA

21 [8]Department of Medical Informatics and Clinical Epidemiology, Oregon Health & Science

22 University, Portland, OR, USA

23 [9]Oregon Clinical and Translational Research Institute, Oregon Health & Science University,

24 Portland, OR, USA

25 [10]Lineberger Comprehensive Cancer Center, University of North Carolina at Chapel Hill, Chapel

26 Hill, NC, USA

27 [11]Department of Pathology and Laboratory Medicine, University of North Carolina at Chapel Hill,

28 Chapel Hill, NC

29 [12]Department of Molecular Microbiology, Washington University School of Medicine, St. Louis,

30 MO, USA

31 [13]Department of Microbiology and Immunology, University of North Carolina at Chapel Hill, Chapel

32 Hill, NC, USA

33 [14]Department of Microbiology and Immunology, University of Texas Medical Branch, Galveston,

34 TX, USA

35   [15]Institute for Human Infection and Immunity, University of Texas Medical Branch, Galveston TX,

36   USA

37   [16]Department of Pathology and Center for Biodefense & Emerging Infectious Diseases, University

38   of Texas Medical Branch, Galveston, TX, USA

39   [17]Rapidly Emerging Antiviral Drug Discovery Initiative, University of North Carolina, Chapel Hill

40   NC, USA

41

42   * Co-first authors

43   + Co-senior authors

44

45

46   **Abstract**

47   Sarbecovirus (CoV) infections, including Severe Acute Respiratory CoV (SARS-CoV) and SARS-

48   CoV-2, are considerable human threats. Human GWAS studies have recently identified loci

49   associated with variation in SARS-CoV-2 susceptibility. However, genetically tractable models

50   that reproduce human CoV disease outcomes are needed to mechanistically evaluate genetic

51   determinants of CoV susceptibility. We used the Collaborative Cross (CC) and human GWAS

52   datasets to elucidate host susceptibility loci that regulate CoV infections and to identify host

53   quantitative trait loci that modulate severe CoV and pan-CoV disease outcomes including a major

54   disease regulating loci including *CCR9. CCR9* ablation resulted in enhanced titer, weight loss,

55   respiratory dysfunction, mortality, and inflammation, providing mechanistic support in mitigating

56   protection from severe SARS-CoV-2 pathogenesis across species. This study represents a

57   comprehensive analysis of susceptibility loci for an entire genus of human pathogens conducted,

58   identifies a large collection of susceptibility loci and candidate genes that regulate multiple aspects

59   type-specific and cross-CoV pathogenesis, and also validates the paradigm of using the CC

60   platform to identify common cross-species susceptibility loci and genes for newly emerging and

61   pre-epidemic viruses.

62

63   **Main Text**

64   Natural host genetic variation regulates disease severity following most viral infections, yet the

65   specific genes and loci that regulate differential disease outcomes are largely unknown across

66   susceptible species[1,2]. Coronaviruses (CoVs) are significant human and animal pathogens; six

67   CoVs (three human, three swine) have emerged or expanded their geographic range in the 21st

68   century[3,4]. The most impactful emergent human CoVs (SARS-CoV and SARS-CoV-2) are group

69   2B coronaviruses, which likely emerged from bats to cause worldwide human epidemic or

70   pandemic respiratory infections, leading to substantial morbidity and mortality[5,6]. Moreover, many

71   high-risk group 2B Sarbecoviruses (SARS-like viruses) and group 2C MERS-like bat CoVs are

72   poised for future human emergence events[7-9]. The Sarbecovirus subgenus is clustered into four

73   clades that include the clade I SARS-CoV and high-risk SARS-like Bat CoVs (BtCoV), clade II

74   SARS-like BtCoVs like HKU3, and clade III SARS-CoV-2 (**Figure 1a**)[10]. Sarbecoviruses vary

75   widely in their ability to cause human and animal disease[11]. SARS-CoV caused ~8,000 infections

76   with a 10% mortality rate, while SARS-CoV-2 has infected ~132 million, leading to ~2.9 million

77   deaths to date[12,13]. SARS-CoV-2 infections cause asymptomatic to life-threatening disease

78   outcomes, supporting a role for inter-host genetic control of emerging viral disease outcomes in

79   both humans and mice[14-16]. Thus, understanding the functions of natural host variants in genes

80   that regulate susceptibility and disease severity after diverse Sarbecovirus infections may reveal

81   common genetic loci that regulate wildtype and variant virus pathogenic outcomes across

82   species, inform threat potential, and reveal novel targets for therapeutic intervention.

83

84   The angiotensin-converting enzyme 2 (ACE2) receptor interacts with the Spike protein (S)

85   receptor binding domains of SARS-CoV, SARS-CoV-2 and many BtCoV Sarbecoviruses, but not

86   the clade II HKU3 strain (**Figure 1b**)[17] As many of these strains do not produce disease in mice,

87   reverse genetics and serial passaging were used to select for SARS-CoV-MA15 (SARS-MA),

88   HKU3-MA, and SARS-CoV-2 MA10 strains that replicate efficiently and produce severe disease

89   in mice[11,18,19,20]. Mouse genetic reference populations (GRPs) have been employed as highly

90   relevant models of human disease, and coupled with systems genetics data algorithms, to identify

91   host susceptibility loci, genes, genetic networks and higher-level genetic interactions that regulate

92   phenotypic variation and disease severity[21-23]. Among these mouse GRPs, the Collaborative

93   Cross (CC) genetic reference population encodes over 44 million single nucleotide

94   polymorphisms (SNPs), 4 million insertions and deletions (InDels), as well as several thousand

95   novel variants (both SNPs as well as InDels) present in single strains[24,25]. Building from our prior

96   work, genetically mapping quantitative trait loci in incipient mice from CC strains (Pre-CC[26], **Table**

97   **1**), we designed a panel of 115 F1 crosses between different CC strains (CC-RIX; an outbred

98   population, like humans, but reproducible (**Figure 1c**)) to identify loci controlling Sarbecovirus

99   pathogenesis and adaptive immune responses. We used our mouse-adapted CoV models,

100 including SARS-CoV MA15 (SARS-MA), HKU3-MA, and SARS-CoV-2 MA10, which replicate

101 efficiently and produce severe disease in mice[11,18,19,20], to overcome the host-specific angiotensin-

102 converting enzyme 2 (ACE-2) interaction with CoV Spike protein.

103

104 **Results**

105 **Phenotypic distributions, genomics scans, and allele effects maps for 3 traits across the**
106 **CC-RIX.**

107 We infected the CC-RIX population with two genetically distinct Sarbecoviruses, which included
108 the clade I SARS-MA and clade II HKU3-MA strains, respectively (**Figure 1a-b**)[11,27]. Groups of
109 CC-RIX mice were inoculated with 5×10^3 plaque-forming units (PFU) of SARS-MA, and viral
110 burden, clinical disease (*e.g.*, weight loss, mortality, and respiratory function), antibody titers, and
111 immune cell infiltrates were measured at multiple timepoints post-infection (ranging from 2-32
112 days) (**Figure 1d, Figure 2**). A matched cohort of CC-RIX was inoculated with 1×10^5 PFU of
113 HKU3-MA and evaluated for mortality and weight loss through day 4 post infection (**Figure 2a**).
114 In both studies, virus challenge elicited an array of disease phenotypes, ranging from clinically
115 inapparent infection to lethal outcomes within the first 4 days of infection. We estimated genetic
116 contributions for many of these traits and determined that heritability for these responses was
117 44.4%-80.9%, estimates that agree with previous CC studies[26,28-31]. Importantly, the various CC-
118 RIX disease phenotypes measured in response to infection appeared relatively uncorrelated
119 (**Figure 2a-c**), suggesting that there are many independent genetic factors driving these
120 responses. We next conducted genetic mapping to identify both genomic regions and specific
121 founder haplotypes driving various aspects of SARS-MA and HKU3-MA disease responses.
122 Given the likely complex genetic architecture underlying these phenotypes, we identified those
123 loci surpassing community-accepted significance thresholds (p<0.33), with distinct allele effects
124 (**Figure 2a-c, Table 1**)[32]. We identified 11 distinct and high-confidence loci in our RIX population
125 affecting weight loss, mortality, titer, antibody responses or respiratory function after SARS-MA
126 infection or weight loss and mortality following HKU3-MA infection. The effect sizes of these loci
127 varied from 3-23% of the total trait variation (that is, largely moderate effect sizes), the loci were
128 located in different genomic regions with different causal founder alleles, and most loci primarily
129 impacted one or a few traits in this population (**Table 1**). The number of independent loci and their
130 trait-specific impacts are consistent with our earlier observations of little to no correlation between
131 disease states across the RIX lines (**Figure 2a-c**). Together, this analysis highlights the genetic
132 complexity driving CoV disease outcomes and immunity and also the inability of any single animal
133 model of CoV disease to fully address all aspects of the disease response.

134

135 To investigate the possibility of pan-sarbecovirus susceptibility loci, we evaluated whether any of
136 our SARS-MA phenotypes also were associated with the haplotypes driving HKU3-MA mortality

137   (**Figure 2d**, **Table 1**). For these analyses, we binned CC-RIX lines based on their diplotypes at

138   these HKU3-MA diseases associated loci, then determined whether these diplotype bins provided

139   an improved fit to the relationship between SARS-MA phenotypes and the CC-RIX IDs

140   themselves. For example, was there any genetic signal at quantitative trait loci (QTL) *HrS10* or

141   *HrS11* that was associated with differential SARS-MA disease when simplifying the underlying

142   causal model; a method we have used to find additional QTLs with small effect sizes in genetically

143   complex populations[29]. *HrS10* was associated with enhanced SARS-MA weight loss, disease and

144   mortality at day 2 post-infection (2 dpi), whereas *HrS11* had moderate associations with SARS-

145   MA lung titers at both 2 and 4 dpi (**Figure 2d**). These results indicate that common susceptibility

146   loci regulate disease severity across two genetically distinct Sarbecovirus clades, and that *HrS10*

147   and *HrS11* are both associated with HKU3-MA-induced mortality, but likely contribute to virus-

148   induced disease through different mechanisms.

149

150   **Disease phenotypes in parental strains CC011 and CC074 and identification of a**

151   **quantitative multitrait locus on chromosome 9 in the CC011xCC074-F2.**

152   Concurrent with our large CC-RIX screen, we identified a pair of inbred CC strains showing highly

153   divergent susceptibilities to SARS-CoV: the disease resistant CC011/Unc and the highly

154   susceptible CC074/Unc strain (CC011 and CC074 from here on, respectively). After challenge

155   with $1x10^4$ PFU SARS-MA, these strains exhibited marked differences in clinical and virological

156   disease phenotypes (*e.g.*, hemorrhage, weight loss, virus titer, mortality, circulating immune

157   cells), and all CC074 mice developed lethal disease by 4 dpi post infection (**Figure 3a, left panel**).

158   Relevant for the current pandemic, these parental strains showed similar severe infection

159   phenotypes during SARS-CoV-2 MA10 infection (**Figure 3a, right panel, Figure S1**). We

160   generated 403 F2 mice by intercrossing these strains (**Figure S2**) and inoculated them

161   intranasally at 9-12 weeks with $1x10^4$ PFU of SARS-MA. These F2 mice showed an expanded

162   range of disease responses relative to their parent CC strains, including mortality, weight loss,

163   titer, respiratory function, circulating immune cell and hemorrhage phenotypes (**Figure S3, Figure**

164   **3b**). We conducted QTL mapping in these F2 mice and identified five significant QTL segregating

165   in this population (*HrS24-28*, **Table 1**), and supply information on other potential loci (p<0.33,

166   **Table S1**). Most of these loci impacted multiple aspects of the SARS-MA disease response during

167   this infection time course (for example analysis of *HrS26* on chromosome 9 indicated the locus

168   contributed to mortality at 4 dpi (Odds ratio (OR) of 3.15), as well as lung hemorrhage or

169   congestion (10.2% of population variation), airflow restriction at 2 dpi (7.8% PenH), as well as

170   peripheral neutrophil (11.8%) and lymphocyte (12.4%) levels) at 4 dpi (**Figure 3c, Table 1**).

171   Recently, three Genome-wide Association Study (GWAS) in humans identified a locus associated

172   with respiratory failure. This locus (encompassing genes such as *SLC6A20*, *LZTFL1*, *FYCO1*,

173   *CXCR6*, *XCR1,* and *CCR9)* is syntenous with a more proximal region of our chromosome 9

174   locus[33-35]. *CCR9* emerged as a strong candidate based on the integration of our data with these

175   studies and the presence of nonsynonomous SNPs in *CCR9* as well as synonymous mutations

176   in regulatory flanking sequences.

177

178   **Identification of *CCR9* as a major susceptibility allele during SARS-CoV-2 infection.**

179   To better understand how our contrasting CC strains and this locus regulates SARS-CoV-2

180   disease, we inoculated CC011, CC074, C57BL/6NJ and *CCR9*^{-/-} mice on a C57BL/6NJ

181   background with SARS-CoV-2 MA10[20]. CC011 and CC074 mice infected with SARS-CoV-2

182   MA10 showed concordance in their SARS- MA disease response phenotypes, including lethality

183   in the CC074 susceptible line. The *CCR9*^{-/-} mice developed more severe clinical disease (**Figure**

184   **4a, Figure S4a**), exhibited increased virus titers (**Figure 4b**), weight loss, mortality and prolonged

185   pulmonary dysfunction and severe lung pathology as measured by whole body plethysmography

186   (**Figure 4c**), lung hemorrhage (**Figure S4b**), and lung damage (**Figure S4c, d and Figure S4e**)

187   relative to their wild-type controls, supporting its important role in protection from disease.

188   Analysis of the cytokine profile in lungs and serum by multiplex immune-assay showed increased

189   subsets of cytokines and chemokines that are involved in promoting allergic airway inflammation,

190   including IL9, IL13, Il17, CCL2, CCL3, CCL5, G-CSF, and Eotaxin either in the lung tissue, serum,

191   or both (**Figure 4f and Figure S5b**). By flow cytometric analysis, the composition of infiltrating

192   cells into the lung tissue (**Figure 4e**) and bronchoalveolar (BAL) fluid (**Figure S5a**) of *CCR9*^{-/-}

193   mice showed a significant increase of CD4^{+} T cells, CD8^{+} effector T cells, inflammation-promoting

194   CD11^{+} DCs and eosinophils at 6 dpi, consistent with an allergic airway inflammatory response.

195   Although originally found to play an important role in chronic gut inflammation, *CCR9* is mainly

196   expressed on lymphocytes, dendritic cells (DCs) and monocytes/macrophages[36,37], and also

197   participates in early allergic airway inflammation including the migration and proliferation of

198   eosinophils and lymphocytes[38]. In addition *CCR9*^{+} DCs are implicated in regulating inflammation,

199   alloimmunity, and autoimmunity[36]. *CCR9*^{-/-} mice develop chronic inflammatory responses and

200   CD11b^{+} inflammatory macrophages contribute to the pathogenesis of liver fibrosis via the

201   *CCR9/CCL25* axis[39,40]. As inflammatory macrophages contribute significantly to increased SARS-

202   CoV pathogenesis in mice[41], together, these data target the *CCR9/CCL25* axis as a major driver

203   of SARS-CoV-2 pathogenesis across species and validate *CCR9* as a driver of the human Chr3

204   susceptibility loci and mouse Chr9 susceptibility locus.

205   A key goal in animal studies is to identify relevant models of human disease. Syntenic genome
206   regions between humans and rodents often regulate a number of infectious and chronic diseases,
207   and our analysis of *HrS26* extends this important pattern[42-44] to sarbecovirus infections. All told,
208   the synteny between human Chr3 and mouse Chr9, the effect sizes of the loci identified in this F2
209   (between 5-15% of the population-wide phenotypic variation in this F2, **Table 1**), as well as the
210   prevalence of loci impacting multiple aspects of SARS-MA associated disease, highlight how
211   sorting of multiple susceptibility alleles into individual CC strains model unique aspects of the
212   genetic control of disease responses. Furthermore, the presence of alleles of at least six of the
213   CC founder strains segregating across these loci (and often in opposite directions: a C57BL/6J
214   allele is protective at *HrS26* and *HrS27* but exacerbating at *HrS28,* **Table 1**) highlights the utility
215   of using genetically complex but reproducible models of disease.
216

217   **Identification of major effect locus on chromosome 4 and of *Trim14* as a susceptibility**
218   **gene during SARS-MA and SARS-CoV-2 MA10 infection.**
219   Next, we revisited a previous CC-F2 intercross, CC003/UncxCC053/Unc (named CC003 and
220   CC053 from here on) conducted by our group[45], and utilized our refined analysis pipelines once
221   the original SARS-MA disease loci (*HrS5-9*) were statistically accounted for. This re-analysis
222   allowed us to identify an additional locus (*HrS23* on chr4) impacting both weight loss and
223   hemorrhagic damage to the lungs as determined by gross pathology (**Figure 5a, b**), as well as
224   several other suggestive QTLs (**Table S1**). The chr4 locus also overlapped with the mortality QTL
225   *HrS24* identified in CC011xCC074-F2 cross (**Figure 5c**). SNP variation between CC003 and
226   CC053, as well as between CC011 and CC074 in this locus pointed to *Trim14* as a likely candidate
227   gene driving these differences in SARS-CoV disease. Previous work identified *Trim14* as a key
228   docking platform in the context of MAVS signaling[46,47]. We used CRISPR/Cas9 targeting to edit
229   *Trim14* in C57BL/6J mice, create a functional knockout (**Figure S6**), and evaluate its role following
230   infection (**Figure 5d, top panel**). *Trim14$^{\Delta47/\Delta47}$* mice inoculated with 1x10^5 PFU of SARS-MA had
231   a modest increase in pathogenesis relative to C57BL/6J control mice. At 3 and 4 dpi, *Trim14*-
232   deficient mice had increased weight loss, which corresponded with increases in viral titer within
233   the lung at 2 and 4 dpi. This result show that an absence of *Trim14* affects viral clearance.
234   Similarly, *Trim14$^{\Delta47/\Delta47}$* mice inoculated with SARS-CoV-2 MA10 also sustained modest increases
235   in weight loss and a delayed recovery phenotype when compared to C57BL/6 mice (**Figure 5d,**
236   **bottom panel**). However, the difference in viral titer seen at early times post SARS-MA infection
237   was not observed with SARS-CoV-2 MA10. Together, these data suggest that Trim14 has a
238   shared role in attenuating Sarbecovirus disease potential, but that this effect varies between

239 viruses. Taken together, the data demonstrates the potential of identifying common and shared

240 QTLs among group 2B coronaviruses.

241

242 **Discussion**

243 Across these studies, we describe several dozen loci impacting different disease responses,

244 including several which show broad responses to all tested Sarbecoviruses. We demonstrate

245 connections to human GWAS studies, and as such these data represent a resource for future

246 comparative studies of Sarbecovirus pathogenesis between humans and animals. Our study

247 highlights the power of using animal GRPs to understand the role of host genetic variation on

248 infectious diseases, generate new models of differential disease, probe the role of individual

249 genes in disease progression, and provide mechanistic insight into the role of specific host genes

250 and viral strains in regulating pathogenesis across species. In appropriately selected large

251 population screens, highly penetrant genetic variants can be identified easily, as can their impacts

252 on specific aspects of disease outcome. In contrast, targeted mapping crosses between highly

253 discordant strains can help to identify more complex genetic interaction networks such as variants

254 that are penetrant only in the context of specific genetic backgrounds, or epistatic (gene-gene)

255 interaction networks.

256

257 We leveraged large-scale population mapping as well as focused intercrosses to better

258 characterize the genetic susceptibility landscape of Sarbecovirus infections in mouse models[26,45]

259 and demonstrated that a large number of polymorphic loci (**Figure 6**) regulate the host disease

260 responses to this subgroup of coronaviruses. Moreover, in this study and others, we have

261 identified specific genes (*Trim55*[26], *Ticam2*[45], and here *Trim14* and *CCR9*), which have naturally

262 occurring polymorphisms driving aberrant SARS-CoV disease responses. Importantly, we

263 demonstrate that *HrS10* and *HrS11* influence disease severity following both clade I SARS-MA

264 and clade II HKU3-MA infection in the CC-RIX, supporting the hypothesis that intrinsic virulence

265 properties encoded within the Sarbecoviruses are subject to similar susceptibility loci in mammals.

266 Further, the concordant susceptibility profiles of CC011, CC074, *Trim14* and *CCR9* deficient mice

267 with SARS-MA and SARS-CoV-2 MA10 highlight the utility of pre-emergence disease models.

268 Such findings are consistent with the discovery that group I and II human norovirus infection and

269 pathogenesis are heavily regulated by polymorphisms in fucosyltransferase 2 (FUT2)[48]. Rich and

270 complex datasets like the ones described here enable comparisons with human GWAS studies

271 mapping QTL after SARS-CoV-2 infection[33-35]. The CC platform can be used to evaluate the role

272 of these loci in mouse models. One advantage of our approach is the use of different mapping

273   platforms, which provide opportunities to combine datasets across projects to gain a greater
274   understanding of the role of how host genetic variation modulates CoV disease responses in
275   mammals (**Figure 6, Table 1**). In addition, the unexplained heritability and suggestive loci (**Table**
276   **S1**) we have identified, suggests that CoV disease and immunity are complex polygenic traits,
277   with the accumulation of variants across many loci driving final disease susceptibility. Collectively,
278   these studies represent the most comprehensive analysis of susceptibility loci for an entire genus
279   of human pathogens, identify a large collection of susceptibility loci and candidate genes that
280   regulate multiple aspects type-specific and cross-CoV pathogenesis, validate a role for the CCR9-
281   CCL25 axis in regulating SARS-CoV-2 disease severity and provide a resource for community
282   wide studies.

283

284   **Figure Legends**
285   **Figure 1. Coronavirus and host- genetic model systems: a-b. Spike phylogeny of**
286   **representative coronaviruses and RBD alignments SARS-CoV, HKU3, and SARS-CoV-2**
287   **with emphasize on ACE2 binding residues**; **c.-d. The RIX Collaborative Cross Screen: The**
288   **design of CC-RIX panel and the phenotypic distribution of disease phenotypes after SARS-**
289   **MA and HKU3-MA infection in the CC-RIX panel**
290   **a.** The Spike protein sequences of selected coronaviruses were aligned and phylogenetically
291   compared. Coronavirus genera are grouped by classic subgroup designations (1a-b, 2a-d, 3, and
292   4). PECoV is designated as 1b* because of its distinctive grouping compared with more
293   conserved proteins. Branches in each tree are labeled with consensus support values (in %).
294   Sequences were aligned using free end gaps with the Blosum62 cost matrix, and the tree was
295   constructed using the neighbor-joining method based on the multiple sequence alignment in
296   Geneious Prime. Numbers following the underscores in each sequence correspond to the
297   GenBank Accession number. **b.** Spike receptor-binding domain (RBD) alignments were
298   performed in Geneious using free end gaps with the Blosum62 cost matrix, and 14 ACE2-critical
299   interacting residues are highlighted in the chart. Residues in the chart are color-coded based on
300   conservation to the SARS-CoV residue (conservation based on Blosum62). **c.** The Collaborative
301   Cross is an octo-parental genetic reference panel. The population captures ~40 million SNPs and
302   small InDels without blind spots across the genome. Each individual strain's unique combination
303   of haplotypes across the genome results from the independent recombinations each strain
304   experienced in their generation. As such, each CC strain represents a unique combination of
305   Coronavirus susceptibility alleles. **d.** Phenotype distribution in CC-RIX panel during SARS-MA
306   infection. Each dot represents the mean of individual CC-RIX strains.

307

308 **Figure 2. Phenotypic distributions, genomics scans, and allele effects maps for 3 traits**

309 **across the CC-RIX.**

310 **a.** *HrS13*, SARS-CoV lung titer at 2 dpi, *HrS11*, percentage survival following HKU3-MA infection,

311 and *HrS12*, weight loss at 4 dpi with HKU3-MA. For all 3 panels, CC-RIX strains are sorted by

312 ascending 2 dpi SARS-MA lung titers, showing the general lack of correlation between

313 coronavirus disease responses. **b.** Genome scans showing the LOD traces, as well as

314 significance thresholds (p=0.33 (orange) and p=0.2 (green)) for the same traits listed above. We

315 identified *HrS13* (ch16) for SARS-CoV titer, *HrS11* (chr5) and *HrS10* (chr13) for HKU3-MA

316 mortality, and *HrS12* for HKU3-MA weight loss. **c.** Allele effects at each of these loci showing

317 causal haplotypes for *HrS13* (where 129S1/SvImJ (pink) and PWK/PhJ (red) alleles cause a

318 reduced titer, *HrS10* where CAST/EiJ (green) and PWK/PhJ (red) alleles cause increased

319 mortality, *HrS11* where a 129S1/SvImJ (pink) allele causes increased mortality, and *HrS12* where

320 a PWK/PhJ (red) allele causes decreased weight loss. **d**. We identified relationships between

321 *HrS10* and SARS-related weight loss and clinical disease (shown is weight loss at 5 dpi), as well

322 as *HrS11* and SARS-MA titer (shown here is titer at 2 dpi), 0 = low response haplotype, 1 = 1

323 copy of the high response/PWK haplotype. Each dot represents data from an individual animal.

324

325 **Figure 3**. **Disease phenotypes in parental strains CC011 and CC074 and identification of a**

326 **quantitative multitrait locus on chromosome 9 in the CC011xCC074-F2.**

327 **a.** CC011 and CC074 were identified as parental CC strains for a F2-screen based on their

328 contrasting SARS-MA induced phenotypes. Shown are weight loss, lung viral titer, percentage

329 survival, and lung hemorrhaging following SARS-MA infection (n=6 for CC011 and CC074,

330 respectively) and SARS-CoV-2 MA10 (n=13 for CC011 and n=13 for CC074). **b.** Shown as

331 example is the phenotypic distribution for lung hemorrhage following SARS-MA infection in the

332 CC011xCC074-F2 panel. The genomic scan shows the LOD traces and significance thresholds

333 (p=0.95 (black), p=0.90 (blue), and p=0.50 (green)). The allele effect of the lung hemorrhage

334 phenotype is broken out based on the homozygous CC011 genotype, the homozygous CC074

335 genotype, or the heterozygous genotype (n=234 individual CC011xCC074-F2 mice). **c.** A

336 quantitative multitrait locus with major effect was identified on chr9 (74.9–124 Mb), which affected

337 mortality, weight loss, hemorrhage, lung function, and peripheral hematology. CC011/Unc has a

338 C57BL/6/PWK haplotype and CC074/Unc has an A/J haplotype in this QTL region.

339

340 **Figure 4. Identification of *CCR9* as a major susceptibility allele during SARS-CoV-2**

341 **infection.** Infection of *CCR9*$^{-/-}$ mice with SARS-CoV-2 MA10 showed significant differences in

342 weight loss (**a.**), viral burden in the lung (**b.**), lung function (**c.**), and cytokine/chemokine

343 distribution (**d.**) in the as well as in the compositions of lung infiltrating immune cells (**e.**) (n=19

344 *CCR9*$^{-/-}$ and n=19 C57BL/6NJ; with n=4 for 2 dpi, n=7 for 4 dpi, n=5 for 6 dpi, and n=3 for 14 dpi

345 for weight loss, viral burden, congestion score, multiplex immune-assay and lung pathology;

346 n=8 for lung function testing; n=12 CCR9$^{-/-}$ and n=13 C57BL/6NJ with n=2 each for mock, n=5-6

347 for 4 dpi, and n=5 for 6 dpi for analysis of infiltrating cells). Data were analyzed using two-way-

348 ANOVA (weight loss, lung function) and Mann-Whitney test (titer, congestion score, pathology

349 scores, FACS analysis, and cytokine/chemokine analysis; *p<0.05, **p<0.01.

350

351 **Figure 5. Identification of major effect locus on chromosome 4 and of *Trim14* as a**

352 **susceptibility gene during SARS-MA and SARS-CoV-2 MA10 infection**. **a.** Phenotypic

353 distribution and genomic scan for *HrS23* (4dpi weight loss in CC003xCC053-F2, **b.** *HrS23* (4dpi

354 lung hemorrhage in CC03xCC053-F2), and **c.** *HrS24* (overall mortality in CC011xCC074-F2. **d.**

355 Infection of *Trim14*$^{\Delta47/\Delta47}$ mice with SARS-MA showed significantly more weight loss and an

356 increase in viral load in the lung compared to C57BL/6J mice over the course of a 7-day infection.

357 A similar trend of infection progression was observed in *Trim14*$^{\Delta47/\Delta47}$ mice infected with SARS-

358 CoV-2 MA10; n=10 *Trim14*$^{\Delta47/\Delta47}$ and n=10 C57BL/6J for weight loss and viral load studies with

359 SARS-CoV-2 MA10 studies; data was analyzed via student t test, *p<0.05, **p<0.01, ***p<0.005).

360

361 **Figure 6. Susceptibility map for SARS-MA and HKU3-MA**. Depicted are significant (p=0.95

362 and p=0.90) QTLs in the Pre-CC (striped), CC-RIX (solid), and the CC011xCC074-F2 and

363 CC003cxCC053-F2 screens, respectively (both checkered).

364

365 **Table1. List of significant QTLs**

366

367 **Supplemental Figure Legends**

368 **Figure S1. CC074 show elevated viral titer at 2 dpi.** Lung tissue of SARS-CoV-2 MA10 infected

369 CC011 (n=6 for d2pi and n=13 for d4pi) and CC074 (n=6 for d2pi and n=13 for d4pi) was tittered

370 by plaque assay to detect viral load on d2pi and d4pi.

371

372 **Figure S2 Design of CC011xCC074-F2 cross.** In specific cases, individual CC strains may

373 present extreme outlier phenotypes, suggesting a sorting of multiple susceptibility alleles in this

374   strain. In such cases, a mapping intercross (e.g. an F2) between two extreme strains can reveal

375   a large number of causal loci and interaction networks.

376

377   **Figure S3. Phenotypic distribution of disease phenotypes after SARS-MA infection in the**

378   **CC011xCC074-F2 screen. a.** Lung hemorrhaging, **b.** weight loss at 4 dpi, **c.** lung titer at 4 dpi,

379   **d.** percentage survival, **e.** peripheral blood lymphocytes, **f.** peripheral blood neutrophils, and **g.**

380   PenH lung function. Each dot represents a single animal.

381

382   **Figure S4. *CCR9$^{-/-}$* mice show significant mortality and lung pathology starting by d6pi of**

383   **infection.** Infection of *CCR9$^{-/-}$* mice with SARS-CoV-2 MA10 showed significant differences in

384   mortality (**a.**), congestion score (**b.**), lung pathology (**c.** and **d.**). Representative H&E stains of lung

385   tissue sections are shown for 4, 6, and 14 dpi for *CCR9$^{-/-}$* and C57BL/6NJ, scale bar indicates

386   100μm (**e.**), (n=19 CCR9$^{-/-}$ and n=19 C57BL/6NJ; with n=4 for 2 dpi, n=7 for 4 dpi, n=5 for 6 dpi,

387   and n=3 for 14 dpi congestion score and histopathology scoring. Data were analyzed using log-

388   rank (mortality) and Mann-Whitney test (congestion score and pathology scores), *p<0.05.

389

390   **Figure S5. Infiltrating cells in BAL of *CCR9$^{-/-}$* and C57BL/6NJ mice after SARS-CoV-2**

391   **MA10 infection.** Infection of *CCR9$^{-/-}$* mice with SARS-CoV-2 MA10 showed significant

392   differences in the compositions of lung infiltrating immune cells in BAL (**a.**) as well as in

393   cytokine/chemokine distribution in serum (**b.**) (n=19 CCR9$^{-/-}$ and n=19 C57BL/6NJ; with n=4 for

394   2 dpi, n=7 for 4 dpi, n=5 for 6 dpi, and n=3 for 14 dpi for multiplex immune-assay and n=12

395   CCR9$^{-/-}$ and n=13 C57BL/6NJ with n=2 each for mock, n=5-6 for 4 dpi, and n=5 for 6 dpi for

396   analysis of infiltrating cells). Data were analyzed using Mann-Whitney test, *p<0.05, **p<0.01.

397

398   **Figure S6. Lung tissue from *Trim14$^{Δ47/Δ47}$* mice lacked detectable Trim14 mRNA.** Tissue from

399   *Trim14$^{Δ47/Δ47}$* were found to lack detectable Trim14 mRNA, likely due to nonsense-mediated

400   decay, as measured by RT-qPCR in comparison to littermates.

401

402   **Figure S7. Gating schemes for flow cytometry analysis.**

403

404   **Supplemental Table S1. List of suggestive QTLs.**

405

406   **Acknowledgments**

414

Author contributions

416 A.S., L.E.G., F.P.M.V., S.K.M., M.T.H., V.D.M., M.T.F., R.S.B designed screens and biology
417 experiments; A.S., L.E.G., S.R.L., V.D.M. conducted and characterized infections *in vivo*; A.S.,
418 L.E.G., S.R.L., E.S.W., K.L.J., D.T.S. performed *in vitro* studies and immune cell quantifications;
419 A.S., L.E.G, S.R.L., R.L.G., S.A.M., V.D.M., M.T.F. processed and analyzed data, and generated
420 figures; A.S., B.K.H, M.A.M., S.J., S.C., S.K.M., M.T.F. performed genetic mapping studies;
421 L.A.V., L.B.T., M.S.D. designed and isolated *Trim14*-deficient mice; A.S., L.E.G., V.D.M.
422 performed *in vivo* evaluation of *Trim14*-deficient infected animals; S.A.M. scored pathologic
423 changes in the lungs of infected mice; R.L.G., S.A. isolated recombinant viruses; T.A.B., P.H.,
424 G.D.S., D.R.M. produced CC-RIX and F2 animals, and processed samples for genotyping; L.E.G.,
425 S.R.L., B.K.H, M.A.M., K.L.J., S.J., T.A.B., L.B.T., D.R.M., G.D.S., M.S.D., F.P.M.V., S.K.M.,
426 M.T.H. edited the manuscript; A.S., M.T.F., R.S.B. wrote the manuscript.

427

Competing interests

429 The authors have no competing interests.

430

References

432 1 Ge, D. *et al.* Genetic variation in IL28B predicts hepatitis C treatment-induced viral
433 clearance. *Nature* **461**, 399-401, doi:10.1038/nature08309 (2009).
434 2 McLaren, P. J. *et al.* Polymorphisms of large effect explain the majority of the host
435 genetic contribution to variation of HIV-1 virus load. *Proc Natl Acad Sci U S A* **112**,
436 14658-14663, doi:10.1073/pnas.1514867112 (2015).
437 3 Wang, Q., Vlasova, A. N., Kenney, S. P. & Saif, L. J. Emerging and re-emerging
438 coronaviruses in pigs. *Curr Opin Virol* **34**, 39-49, doi:10.1016/j.coviro.2018.12.001
439 (2019).
440 4 Chen, B. *et al.* Overview of lethal human coronaviruses. *Signal Transduct Target Ther* **5**,
441 89, doi:10.1038/s41392-020-0190-2 (2020).
442 5 Zhou, P. *et al.* A pneumonia outbreak associated with a new coronavirus of probable bat
443 origin. *Nature* **579**, 270-273, doi:10.1038/s41586-020-2012-7 (2020).

444 6   Zhang, Y. Z. & Holmes, E. C. A Genomic Perspective on the Origin and Emergence of
445   SARS-CoV-2. *Cell* **181**, 223-227, doi:10.1016/j.cell.2020.03.035 (2020).
446 7   Menachery, V. D. *et al.* SARS-like WIV1-CoV poised for human emergence. *Proc Natl
447   Acad Sci U S A* **113**, 3048-3053, doi:10.1073/pnas.1517719113 (2016).
448 8   Menachery, V. D. *et al.* A SARS-like cluster of circulating bat coronaviruses shows
449   potential for human emergence. *Nat Med* **21**, 1508-1513, doi:10.1038/nm.3985 (2015).
450 9   Anthony, S. J. *et al.* Further Evidence for Bats as the Evolutionary Source of Middle East
451   Respiratory Syndrome Coronavirus. *mBio* **8**, doi:10.1128/mBio.00373-17 (2017).
452 10   Coronaviridae Study Group of the International Committee on Taxonomy of, V. The
453   species Severe acute respiratory syndrome-related coronavirus: classifying 2019-nCoV
454   and naming it SARS-CoV-2. *Nat Microbiol* **5**, 536-544, doi:10.1038/s41564-020-0695-z
455   (2020).
456 11   Becker, M. M. *et al.* Synthetic recombinant bat SARS-like coronavirus is infectious in
457   cultured cells and in mice. *Proc Natl Acad Sci U S A* **105**, 19944-19949,
458   doi:10.1073/pnas.0808116105 (2008).
459 12   Ahmad, T., Haroon, Baig, M. & Hui, J. Coronavirus Disease 2019 (COVID-19)
460   Pandemic and Economic Impact. *Pak J Med Sci* **36**, S73-S78,
461   doi:10.12669/pjms.36.COVID19-S4.2638 (2020).
462 13   Enserink, M. & Kupferschmidt, K. With COVID-19, modeling takes on life and death
463   importance. *Science* **367**, 1414-1415, doi:10.1126/science.367.6485.1414-b (2020).
464 14   Rasmussen, A. L. *et al.* Host genetic diversity enables Ebola hemorrhagic fever
465   pathogenesis and resistance. *Science* **346**, 987-991, doi:10.1126/science.1259595 (2014).
466 15   Sanchez, A., Wagoner, K. E. & Rollin, P. E. Sequence-based human leukocyte antigen-B
467   typing of patients infected with Ebola virus in Uganda in 2000: identification of alleles
468   associated with fatal and nonfatal disease outcomes. *J Infect Dis* **196 Suppl 2**, S329-336,
469   doi:10.1086/520588 (2007).
470 16   Cameron, M. J. *et al.* Interferon-mediated immunopathological events are associated with
471   atypical innate and adaptive immune responses in patients with severe acute respiratory
472   syndrome. *J Virol* **81**, 8692-8706, doi:10.1128/JVI.00527-07 (2007).
473 17   Shang, J. *et al.* Structure of mouse coronavirus spike protein complexed with receptor
474   reveals mechanism for viral entry. *PLoS Pathog* **16**, e1008392,
475   doi:10.1371/journal.ppat.1008392 (2020).
476 18   Roberts, A. *et al.* A mouse-adapted SARS-coronavirus causes disease and mortality in
477   BALB/c mice. *PLoS Pathog* **3**, e5, doi:10.1371/journal.ppat.0030005 (2007).
478 19   Dinnon, K. H. *et al.* A mouse-adapted SARS-CoV-2 model for the evaluation of COVID-
479   19 medical countermeasures. *bioRxiv*, doi:10.1101/2020.05.06.081497 (2020).
480 20   Leist, S. R. *et al.* A Mouse-adapted SARS-CoV-2 induces Acute Lung Injury (ALI) and
481   mortality in Standard Laboratory Mice. *Cell*, doi:10.1016/j.cell.2020.09.050 (2020).
482 21   Leist, S. R. & Baric, R. S. Giving the Genes a Shuffle: Using Natural Variation to
483   Understand Host Genetic Contributions to Viral Infections. *Trends Genet* **34**, 777-789,
484   doi:10.1016/j.tig.2018.07.005 (2018).
485 22   Schafer, A., Baric, R. S. & Ferris, M. T. Systems approaches to Coronavirus
486   pathogenesis. *Curr Opin Virol* **6**, 61-69, doi:10.1016/j.coviro.2014.04.007 (2014).
487 23   Noll, K. E., Ferris, M. T. & Heise, M. T. The Collaborative Cross: A Systems Genetics
488   Resource for Studying Host-Pathogen Interactions. *Cell Host Microbe* **25**, 484-498,
489   doi:10.1016/j.chom.2019.03.009 (2019).

490 24   Srivastava, A. *et al.* Genomes of the Mouse Collaborative Cross. *Genetics* **206**, 537-556,
491   doi:10.1534/genetics.116.198838 (2017).
492 25   Collaborative Cross, C. The genome architecture of the Collaborative Cross mouse
493   genetic reference population. *Genetics* **190**, 389-401, doi:10.1534/genetics.111.132639
494   (2012).
495 26   Gralinski, L. E. *et al.* Genome Wide Identification of SARS-CoV Susceptibility Loci
496   Using the Collaborative Cross. *PLoS Genet* **11**, e1005504,
497   doi:10.1371/journal.pgen.1005504 (2015).
498 27   Frieman, M. *et al.* Molecular determinants of severe acute respiratory syndrome
499   coronavirus pathogenesis and virulence in young and aged mouse models of human
500   disease. *J Virol* **86**, 884-897, doi:10.1128/JVI.05957-11 (2012).
501 28   Maurizio, P. L. *et al.* Bayesian Diallel Analysis Reveals Mx1-Dependent and Mx1-
502   Independent Effects on Response to Influenza A Virus in Mice. *G3 (Bethesda)* **8**, 427-
503   445, doi:10.1534/g3.117.300438 (2018).
504 29   Noll, K. E. *et al.* Complex Genetic Architecture Underlies Regulation of Influenza-A-
505   Virus-Specific Antibody Responses in the Collaborative Cross. *Cell Rep* **31**, 107587,
506   doi:10.1016/j.celrep.2020.107587 (2020).
507 30   Aylor, D. L. *et al.* Genetic analysis of complex traits in the emerging Collaborative
508   Cross. *Genome Res* **21**, 1213-1222, doi:10.1101/gr.111310.110 (2011).
509 31   Ferris, M. T. *et al.* Modeling host genetic regulation of influenza pathogenesis in the
510   collaborative cross. *PLoS Pathog* **9**, e1003196, doi:10.1371/journal.ppat.1003196 (2013).
511 32   Abiola, O. *et al.* The nature and identification of quantitative trait loci: a community's
512   view. *Nat Rev Genet* **4**, 911-916, doi:10.1038/nrg1206 (2003).
513 33   Ellinghaus, D. *et al.* Genomewide Association Study of Severe Covid-19 with
514   Respiratory Failure. *N Engl J Med*, doi:10.1056/NEJMoa2020283 (2020).
515 34   Pairo-Castineira, E. *et al.* Genetic mechanisms of critical illness in Covid-19. *Nature*,
516   doi:10.1038/s41586-020-03065-y (2020).
517 35   Shelton, J. F. *et al.* Trans-ancestry analysis reveals genetic and nongenetic associations
518   with COVID-19 susceptibility and severity. *Nat Genet*, doi:10.1038/s41588-021-00854-7
519   (2021).
520 36   Pathak, M. & Lal, G. The Regulatory Function of CCR9(+) Dendritic Cells in
521   Inflammation and Autoimmunity. *Front Immunol* **11**, 536326,
522   doi:10.3389/fimmu.2020.536326 (2020).
523 37   Wang, C. *et al.* The role of chemokine receptor 9/chemokine ligand 25 signaling: From
524   immune cells to cancer cells. *Oncol Lett* **16**, 2071-2077, doi:10.3892/ol.2018.8896
525   (2018).
526 38   Lopez-Pacheco, C., Soldevila, G., Du Pont, G., Hernandez-Pando, R. & Garcia-Zepeda,
527   E. A. CCR9 Is a Key Regulator of Early Phases of Allergic Airway Inflammation.
528   *Mediators Inflamm* **2016**, 3635809, doi:10.1155/2016/3635809 (2016).
529 39   Nakamoto, N. Role of inflammatory macrophages and CCR9/CCL25 chemokine axis in
530   the pathogenesis of liver injury as a therapeutic target. *Nihon Rinsho Meneki Gakkai*
531   *Kaishi* **39**, 460-467, doi:10.2177/jsci.39.460 (2016).
532 40   Chu, P. S. *et al.* C-C motif chemokine receptor 9 positive macrophages activate hepatic
533   stellate cells and promote liver fibrosis in mice. *Hepatology* **58**, 337-350,
534   doi:10.1002/hep.26351 (2013).

41   Channappanavar, R. *et al.* Dysregulated Type I Interferon and Inflammatory Monocyte-Macrophage Responses Cause Lethal Pneumonia in SARS-CoV-Infected Mice. *Cell Host Microbe* **19**, 181-193, doi:10.1016/j.chom.2016.01.007 (2016).

42   Murdoch, B. M. *et al.* Genome-wide scan identifies loci associated with classical BSE occurrence. *PLoS One* **6**, e26819, doi:10.1371/journal.pone.0026819 (2011).

43   Prisco, S. Z. *et al.* Refined mapping of a hypertension susceptibility locus on rat chromosome 12. *Hypertension* **64**, 883-890, doi:10.1161/HYPERTENSIONAHA.114.03550 (2014).

44   Jamieson, S. E. *et al.* Evidence for a cluster of genes on chromosome 17q11-q21 controlling susceptibility to tuberculosis and leprosy in Brazilians. *Genes Immun* **5**, 46-57, doi:10.1038/sj.gene.6364029 (2004).

45   Gralinski, L. E. *et al.* Allelic Variation in the Toll-Like Receptor Adaptor Protein Ticam2 Contributes to SARS-Coronavirus Pathogenesis in Mice. *G3 (Bethesda)* **7**, 1653-1663, doi:10.1534/g3.117.041434 (2017).

46   Zhou, Z. *et al.* TRIM14 is a mitochondrial adaptor that facilitates retinoic acid-inducible gene-I-like receptor-mediated innate immune response. *Proc Natl Acad Sci U S A* **111**, E245-254, doi:10.1073/pnas.1316941111 (2014).

47   Tan, P. *et al.* Assembly of the WHIP-TRIM14-PPP6C Mitochondrial Complex Promotes RIG-I-Mediated Antiviral Signaling. *Mol Cell* **68**, 293-307 e295, doi:10.1016/j.molcel.2017.09.035 (2017).

48   Lindesmith, L. *et al.* Human susceptibility and resistance to Norwalk virus infection. *Nat Med* **9**, 548-553, doi:10.1038/nm860 (2003).

49   Menachery, V. D., Gralinski, L. E., Baric, R. S. & Ferris, M. T. New Metrics for Evaluating Viral Respiratory Pathogenesis. *PLoS One* **10**, e0131451, doi:10.1371/journal.pone.0131451 (2015).

50   Leist, S. R., Jensen, K. L., Baric, R. S. & Sheahan, T. P. Increasing the translation of mouse models of MERS coronavirus pathogenesis through kinetic hematological analysis. *PLoS One* **14**, e0220126, doi:10.1371/journal.pone.0220126 (2019).

51   Sheahan, T. P. *et al.* Comparative therapeutic efficacy of remdesivir and combination lopinavir, ritonavir, and interferon beta against MERS-CoV. *Nat Commun* **11**, 222, doi:10.1038/s41467-019-13940-6 (2020).

52   Sigmon, J. S. *et al.* Content and performance of the MiniMUGA genotyping array, a new tool to improve rigor and reproducibility in mouse research. *bioRxiv*, 2020.2003.2012.989400, doi:10.1101/2020.03.12.989400 (2020).

53   Gatti, D. M. *et al.* Quantitative trait locus mapping methods for diversity outbred mice. *G3 (Bethesda)* **4**, 1623-1633, doi:10.1534/g3.114.013748 (2014).

54   Broman, K. W., Wu, H., Sen, S. & Churchill, G. A. R/qtl: QTL mapping in experimental crosses. *Bioinformatics* **19**, 889-890, doi:10.1093/bioinformatics/btg112 (2003).

Online Material and Methods

Cells and viruses

Recombinant mouse-adapted SARS-CoV MA15 (SARS-MA), HKU3-SRBD-MA (HKU3-MA), and SARS-CoV-2 MA10 (SARS-2-MA) virus were generated as described previously (HKU3-SRBD-MA: GenBank Accession Number XXX, SARS-CoV-2 MA10: GenBank Accession Number

579   XXX)[11,18,20]. For virus titration, the caudal lobe of the right lung was homogenized in PBS, resulting

580   homogenate was serial-diluted and inoculated onto confluent monolayers of Vero E6 cells (ATCC

581   XXX), followed by agarose overlay. Plaques were visualized with overlay of Neutral Red dye on

582   day 2 (SARS-MA) or day 3 (SARS-CoV-2 MA10) post infection.

583

584   **Mouse studies and *in vivo* infections**

585   All mouse studies were performed at the University of North Carolina (Animal Welfare Assurance

586   #A3410-01) using protocols approved by the UNC Institutional Animal Care and Use Committee

587   (IACUC). Animal studies at Washington University were carried out in accordance with the

588   recommendations in the Guide for the Care and Use of Laboratory Animals of the National

589   Institutes of Health. The protocols were approved by the IACUC at the Washington University

590   School of Medicine (Assurance number A3381-01).

591   Mouse studies fall into three major classes: CC-RIX, F2 intercross mice, and inbred wild-type or

592   gene-edited mice. The laboratory of Pardo Manuel de Villena (FPMV) purchased CC mice from

593   the Systems Genetics Core Facility at UNC between 2012 and 2018. These CC mice were used

594   to breed CC-RIXs in the FPMV laboratory, to ensure proper cohorts and batch sizes. CC-RIXs

595   were generated in a ring design such that each CC-RIX had one copy of the MHC H2B^b allele,

596   and that each CC strain was used as both dam and sire in equal proportion across all RIXs. Mice

597   (~105 CC-RIX strains, 3 animals each) were transferred at 5-6 weeks of age to the Baric (RSB)

598   laboratory for infection between 9-12 weeks of age.

599   The details of the CC003 x CC053 F2 are published[45]. The Systems Genetics Core Facility was

600   contracted to generate the F2 cross between CC011 and CC074. F1 mice between CC011 and

601   CC074 were generated in both potential cross directions, and F2 mice were bred in all 4 possible

602   F1 x F1 combinations, to ensure appropriately balanced sex chromosome and parent-of-origin

603   effects. F2 mice (226 males, 177 females) were weaned such that littermates were randomized

604   to different experimental cages to further reduce litter- or batch-effects on the study, and mice

605   were transferred at 5-6 weeks of age to the RSB laboratory for infection between 9-12 weeks of

606   age.

607   15- week old *CCR9$^{-/-}$* mice (strain 027041) and 15-week old female C57BL/6NJ mice (strain

608   005304) were purchased from Jackson Laboratory. CC-RIX, CC-F2 mice, *Trim14*-deficient, and

609   CCR9$^{-/-}$ mice were infected with 5x10^3 (CC-RIX with SARS-MA), 1x10^4 (CC-F2 with SARS-MA

610   and SARS-CoV-2 MA10), and 1x10^5 (CC-RIX with HKU3-MA, *Trim14$^{\Delta47/\Delta47}$* and *CCR9$^{-/-}$* mice with

611   SARS-MA and SARS-CoV-2 MA10) plaque forming units (PFU) in 50 μl PBS intranasally at 9-12

612   (CC-RIX and CC-F2 mice) or 15 (*CCR9$^{-/-}$* and C57BL/6NJ) weeks of age, respectively. Body

613 weight, mortality, and pulmonary function by whole body plethysmography[49] were monitored daily
614 where indicated. At indicated timepoints, mice were euthanized and gross pathology (hemorrhage
615 score) of the lung was assessed and scored on a scale from 0 (no hemorrhage) to 4 (severe
616 hemorrhage affecting all lung lobes). Then lung tissue was harvested for titer and histopathology
617 analysis; and blood samples were harvested to determine antibody composition and for analysis
618 of peripheral immune cells. Samples were stored at -80°C until homogenized and titered by
619 plaque assay as described above. Serum was prepared and SARS-CoV spike-specific antibody
620 were quantified by ELISA as previously described[33]. Peripheral blood was diluted 1:5 in
621 PBS/EDTA and analyzed with the VetScan HM5 as previously described [50]. Histopathology
622 samples were fixed in 10% phosphate buffered formalin for 7 days before paraffin embedding,
623 sectioning stained with hematoxylin and eosin.

624

625 **Generation of *Trim14*-deficient mice**
626 Gene-edited *Trim14*-deficient mice were generated with support from the Genome Engineering
627 and iPSC center and Department of Pathology Micro-Injection Core (Washington University
628 School of Medicine). A sgRNA targeting exon 4 of *Trim14* was selected based on minimal off-
629 target effects *in silico* and targeting efficiency *in vitro*. The sgRNA (5'-
630 ACCAATGGACACTCGCCTGANGG-3') was synthesized, transcribed (HiScribe T7 *In vitro*
631 Transcription Kit, New England BioLabs), and purified (MEGAclear Transcription Clean-Up Kit,
632 Thermo Fisher). The sgRNA was mixed and co-injected with Cas9 RNA at 5ng/μl and 10ng/μl
633 final concentrations into half-day-old C57BL/6J embryos (E0.5). After next-generation sequencing
634 of founders and two generations of mice backcrossed to C57BL/6J mice, a mouse line with a 47-
635 nucleotide deletion (5'-
636 GCCTGAAGGAAAGTGAGTTGCCTAAGACCAACTCCAAGTCCTTGCTC-3') encompassing the
637 3' splice site of intron 4 and part of the coding region of exon 4 was generated. These $Trim14^{\Delta 47/\Delta 47}$
638 mice were bred as homozygotes and used for experiments. $Trim14^{\Delta 47/\Delta 47}$ mice were born in normal
639 Mendelian frequencies and showed no apparent defects in development, growth, or fecundity.
640 Lung tissue from $Trim14^{\Delta 47/\Delta 47}$ were found to lack detectable *Trim14* mRNA, likely due to
641 nonsense-mediated decay, as measured by RT-qPCR using a predesigned primer/probe set for
642 *Trim14* (IDT, Assay ID Mm.PT.58.286730) and the housekeeping gene *GAPDH* (IDT, Assay ID
643 Mm.PT.39a.1). Sanger sequencing of a polymerase chain reaction amplicon [5'
644 GGCACAGCTCAACCCATGG -3' (forward) and 5'- ACCAGCGAGCTCGTGCTCC -3' (reverse)]
645 was used for genotyping.

646

Flow cytometry analysis of immune cell infiltrates.

For analysis of BAL fluid, mice were sacrificed by ketamine overdose, followed by cannulation of the trachea with a 19-G canula. BAL was performed with three washes of 0.8 ml of sterile PBS. BAL fluid was centrifuged, and single cell suspensions were generated for staining. For analysis of lung tissues, mice were perfused with sterile PBS, and the right inferior lung lobes were digested at 37°C with 630 μg/mL collagenase D (Roche) and 75 U/mL of DNase I (Sigma–Aldrich) for 2 h. Single cell suspensions of BAL fluid and lung digest were preincubated with Fc Block antibody (BD PharMingen) in PBS + 2% heat-inactivated FBS for 10 min at room temperature before staining. Cells were incubated with antibodies against the following markers: efluor506 Viability Dye (Thermo Fisher, 65-0866-14), BUV395 anti- CD45 (Clone 30-F11, BD Biosciences), BV711 anti-CD11b (Clone M1/70, Biolegend), APC-Cy7 anti-CD11c (Clone HL3, BD Biosciences), BV650 anti-Ly6G (Clone 1A8, Biolegend), Pacific Blue anti-Ly6C (Clone HK1.4, Biolegend) FITC anti-CD24 (Clone M1/69, Biolegend), PE anti-Siglec F (Clone E50-2440, Biolegend), PE-Cy7 anti-CD64 (Clone X54-5/7.1, Biolegend), AF700 anti-MHCII (Clone M5/114.15.2, Biolegend), BV421 anti-CD3 (Clone 17A2, Biolegend), BV785 anti-CD4 (Clone GK1.5, Biolegend), APC anti-CD8a (Clone 53-6.7, Biolegend) BV421 anti-B220 (Clone RA3-6B2, Biolegend) APC-Cy7 anti-CD44 (Clone IM7, Biolegend) BV605 anti-CD62L (Clone MEL-14, Biolegend). All antibodies were used at a dilution of 1:200. Cells were stained for 20 min at 4°C, washed, fixed and permeabilized for intracellular staining with Foxp3/Transcription Factor Staining Buffer Set (eBioscience) according to manufacturer's instructions. Cells were incubated overnight at 4°C with BV421 anti-Foxp3 (Clone MF-14, Biolegend) washed, re-fixed with 4% PFA (EMS) for 20 min and resuspended in permeabilization buffer. Absolute cell counts were determined using Trucount beads (BD). Flow cytometric data were acquired on a cytometer (BD-X20; BD Biosciences) and analyzed using FlowJo software (Tree Star) (**Figure S7**).

Cytokine and chemokine protein analysis

The small center lung lobe of each mouse was homogenized in 1 ml of PBS and briefly centrifuged to remove debris. Fifty microliters of homogenate were used to measure cytokine and chemokine protein abundance using a Bio-Plex Pro mouse cytokine 23-plex assay (Bio-Rad) according to the manufacturer's instructions.

Lung pathology scoring

Two separate lung pathology scoring scales, Matute-Bello and Diffuse Alveolar Damage (DAD), were used to quantify acute lung injury (ALI)[51].

681   For Matute-Bello scoring samples were blinded and three random fields of lung tissue were

682   chosen and scored for the following: (A) neutrophils in alveolar space (none = 0, 1–5 cells = 1, >

683   5 cells = 2), (B) neutrophils in interstitial space (none = 0, 1–5 cells = 1, > 5 cells = 2), (C) hyaline

684   membranes (none = 0, one membrane = 1, > 1 membrane = 2), (D) Proteinaceous debris in air

685   spaces (none = 0, one instance = 1, > 1 instance = 2), (E) alveolar septal thickening (< 2Å~ mock

686   thickness = 0, 2–4Å~ mock thickness = 1, > 4Å~ mock thickness = 2). Scores from A–E were put

687   into the following formula score = [(20x A) + (14 x B) + (7 x C) + (7 x D) + (2 x E)]/100 to obtain a

688   lung injury score per field and then averaged for the final score for that sample.

689   In a similar way, for DAD scoring, three random fields of lung tissue were scored for the in a

690   blinded manner for: 1= absence of cellular sloughing and necrosis, 2= uncommon solitary cell

691   sloughing and necrosis (1–2 foci/field), 3=multifocal (3+foci) cellular sloughing and necrosis with

692   uncommon septal wall hyalinization, or 4=multifocal (>75% of field) cellular sloughing and

693   necrosis with common and/or prominent hyaline membranes. To obtain the final DAD score per

694   mouse, the scores for the three fields per mouse were averaged.

695

696   **Genotyping**

697   CC003, CC053, their F1 progeny, and the F2 cross were genotyped as previously described[45].

698   CC011, CC074, their F1 progeny, and the F2 cross were genotyped on the MiniMUGA genotyping

699   array[52]. Genomic DNA was isolated from tail-clips of animals using the Qiagen (Hilden, Germany)

700   DNeasy Blood & Tissue kit. 1.5 µg was sent to Neogen (Lincoln, Nebraska) for processing. We

701   filtered the genotypes upon return for informativeness within this cross. To be considered

702   informative, the marker had to have one homozygous allele in all CC011 mice genotyped, the

703   alternate homozygous allele in all CC074 mice genotyped, and the appropriate call in all F1

704   animals (H calls on the autosomes, an H call in females on the X chromosomes, and the relevant

705   homozygous call in male F1s). This filtering reduced the ~10,800 SNPs on the MiniMUGA array

706   to 2821 informative markers.

707

708   **QTL mapping and statistical analyses**

709   For the CC-RIX, we used the same pipeline we previously described[29]. Briefly, each CC-RIX had

710   their genome represented as an array of probabilities of each of the 8 CC founder haplotypes

711   (**Figure 1C**). This array was used in the DOQTL R package[53] to run an 8-allele regression at each

712   of 77,000 markers for our CC-RIX phenotypes. At each marker, a LOD score is calculated

713   describing the goodness of fit of our trait~genotype model relative to a null model. Significance

714   was determined by running 1000 permutations scrambling the relationship between phenotypes

715   and haplotypes. In this way, significance is independent of both population allele frequencies, as

716   well as the phenotypic distribution. For the F2 crosses, instead of a regression on haplotype

717   probabilities, the R/QTL package conducts a regression of the trait of interest on the exact

718   genotypes at each locus[54]. As with the CC-RIX mapping, permutation testing is used to identify

719   significance.

720

Figure 1
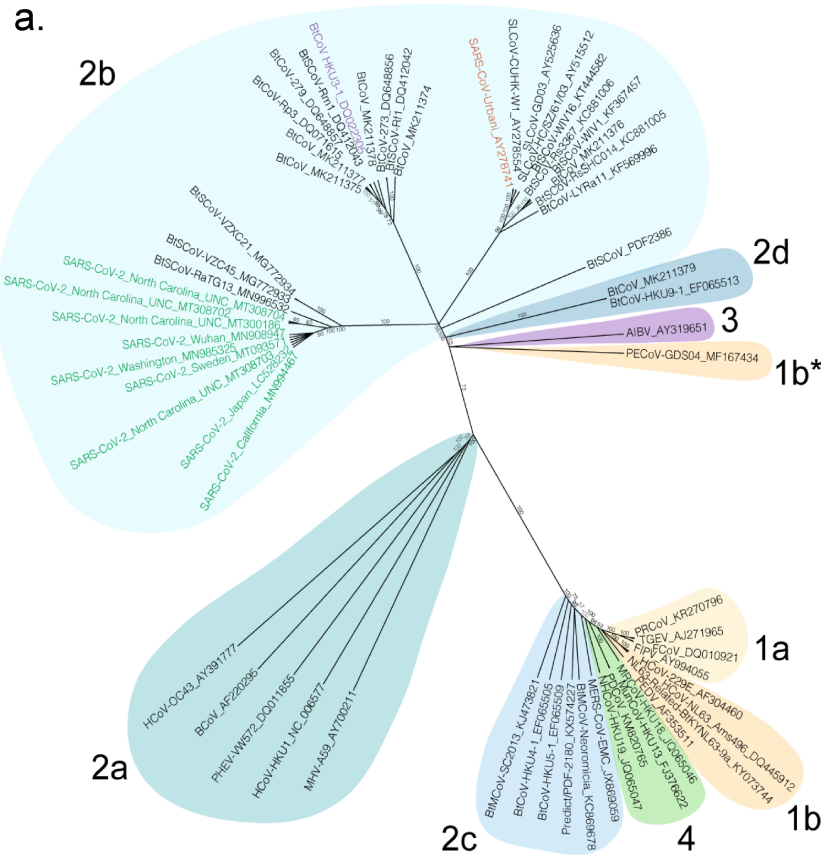
b.

Virus	402	426	436	440	442	472	473	475	479	484	486	487	488	491
SARS-CoV	T	R	Y	Y	Y	L	N	Y	N	Y	T	T	G	Y
SARS-CoV-MA15	T	R	H	Y	Y	L	N	Y	N	Y	T	T	G	Y
BtCoV-HKU3	T	A	-	Y	S	-	-	-	S	N	N	V	P	Y
SARS-CoV-2	T	N	Y	Y	L	F	N	Y	Q	Q	T	N	G	Y

c.

CC strain X **CC strain**

RIX line

d.

percentage survival

d4pi weight loss

d2pi viral load

d2pi PenH function

d2pi Rpef function

d4pi CD8+ DCs

d32pi total IgG

d32pi total IgG1
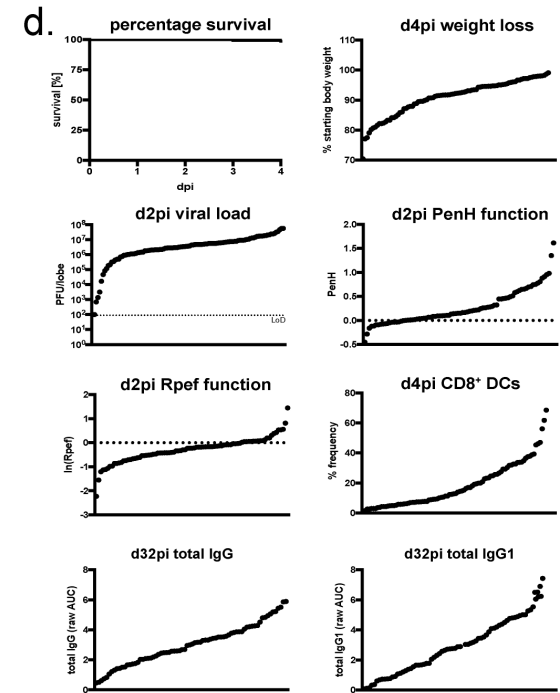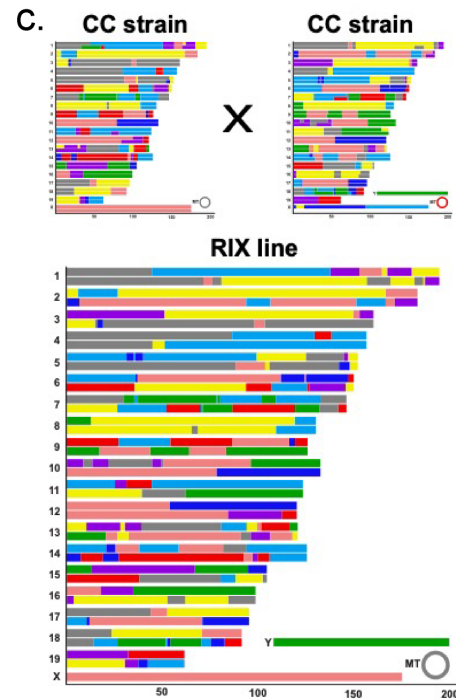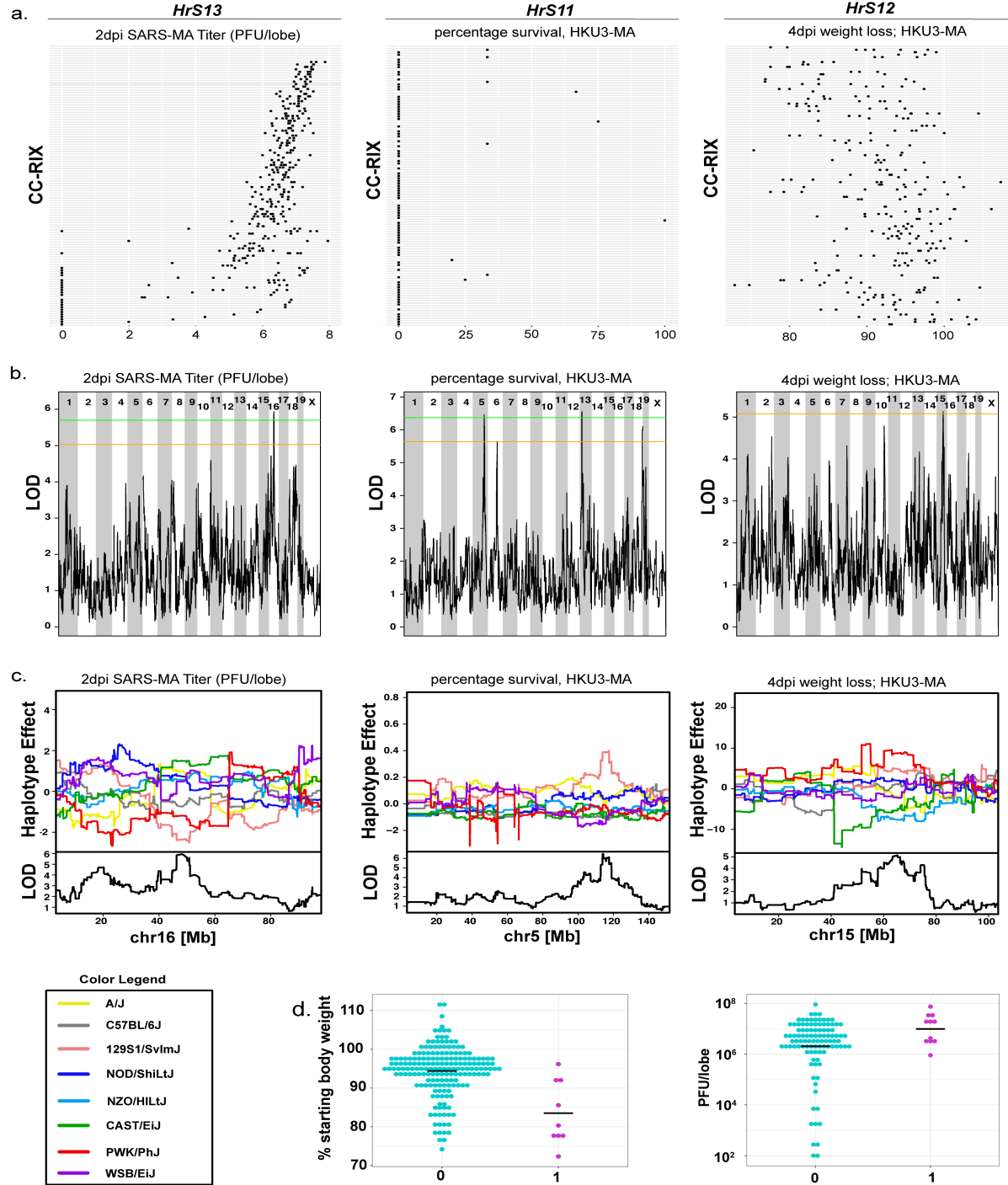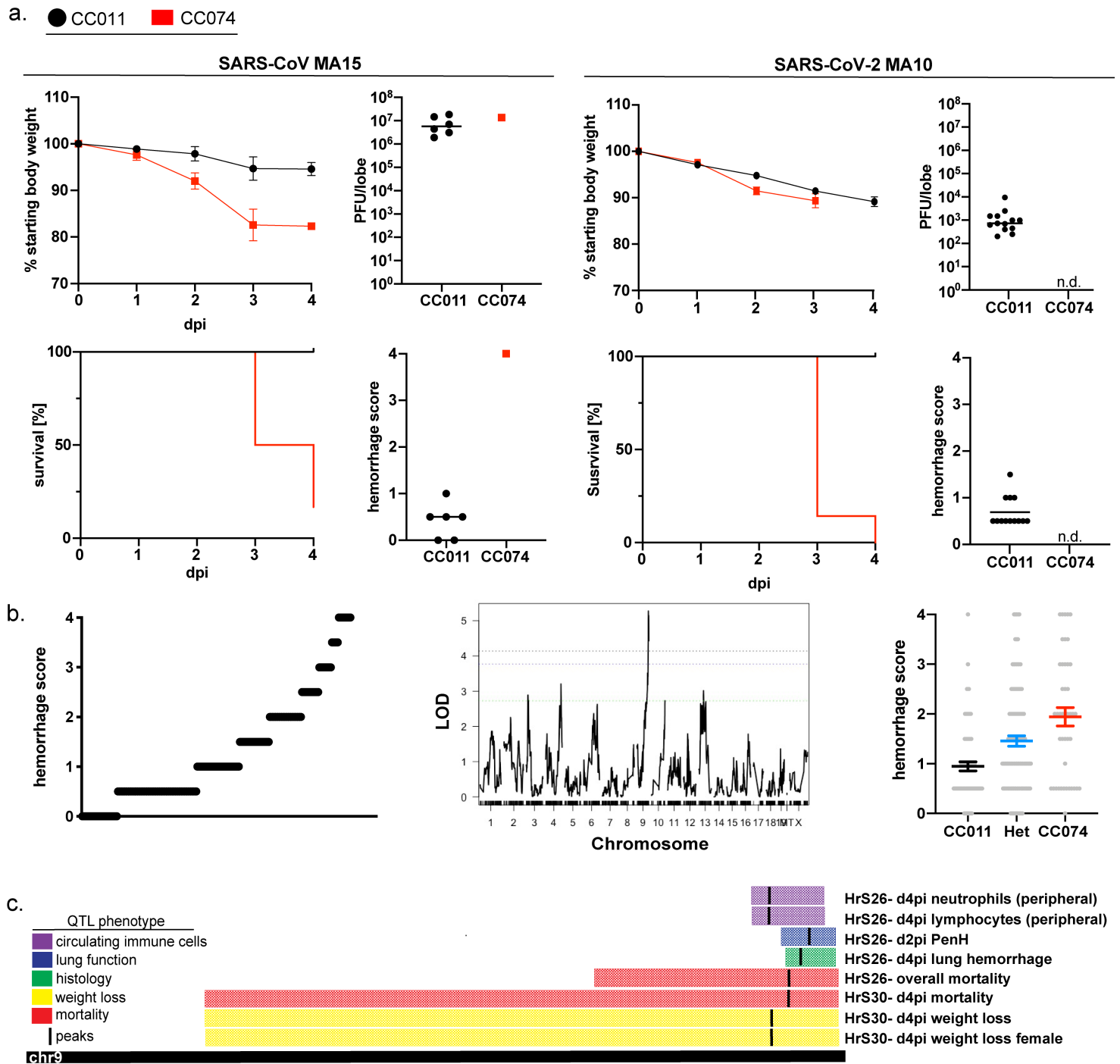
Figure 2

Figure 3

Figure 4
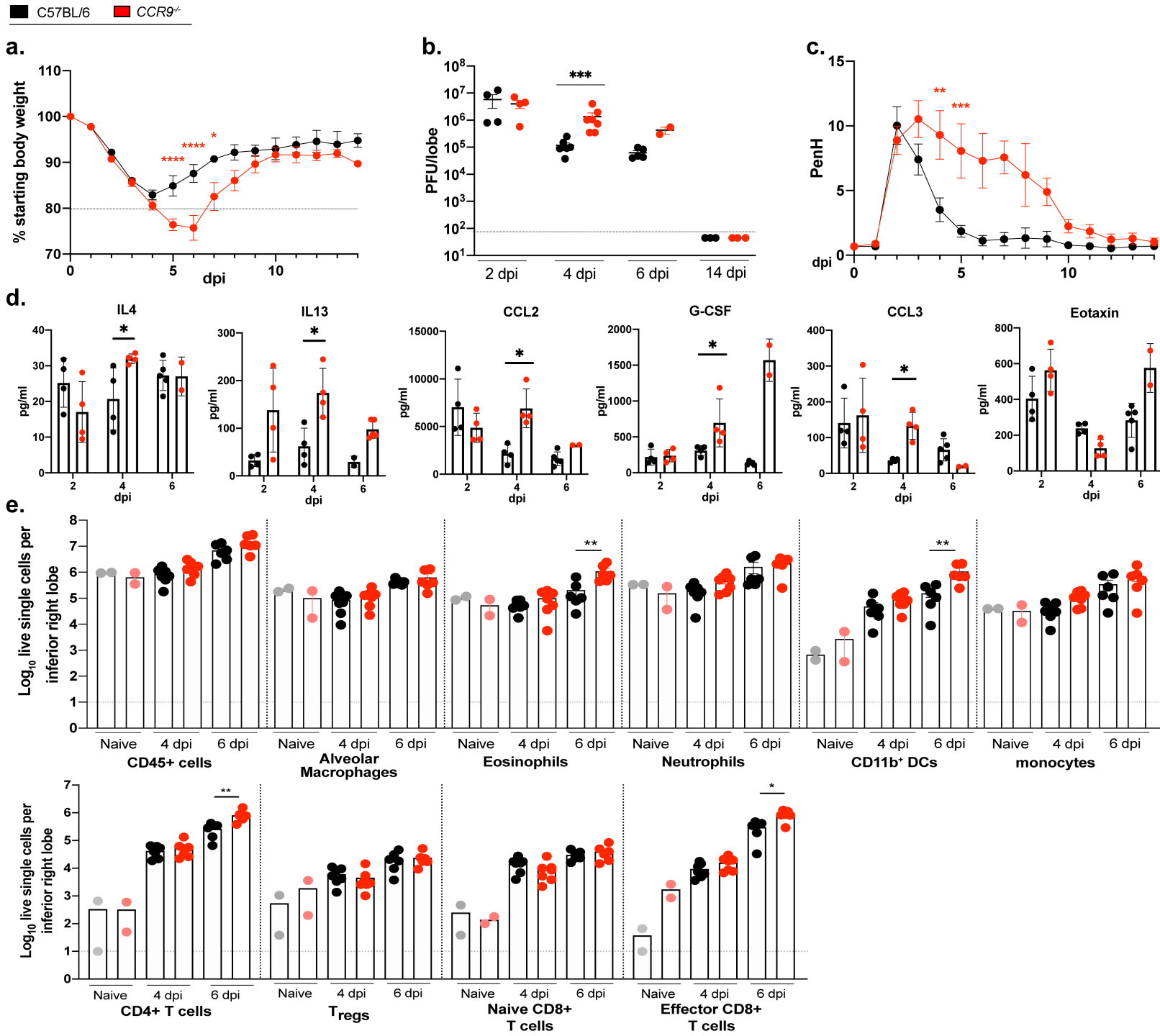
Figure 5

a. *HrS23*: CC003xCC053-F2
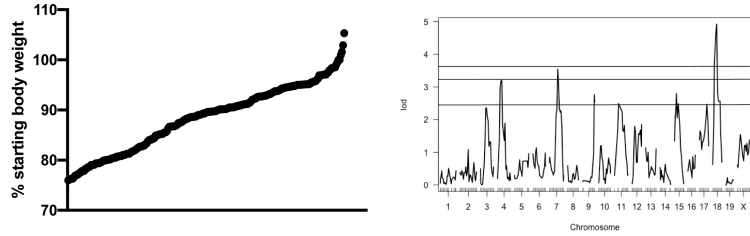
b. *HrS23*: CC003xCC053-F2
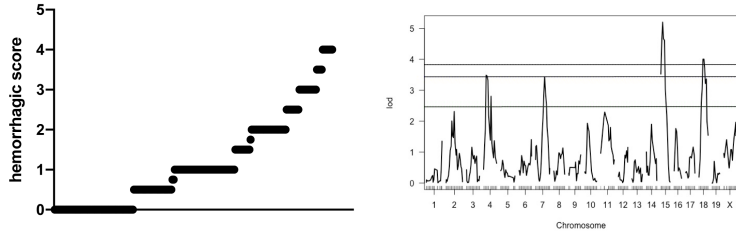
c. *HrS24*: CC011xCC074-F2
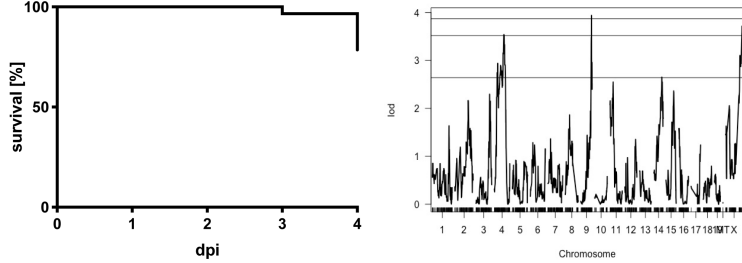
d. ■ C57BL/6   ■ *TRIM14*$^{\Delta47/\Delta47}$

SARS-CoV MA15
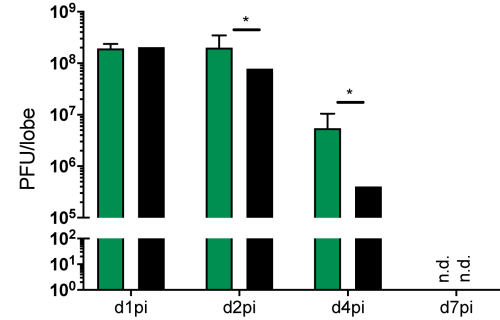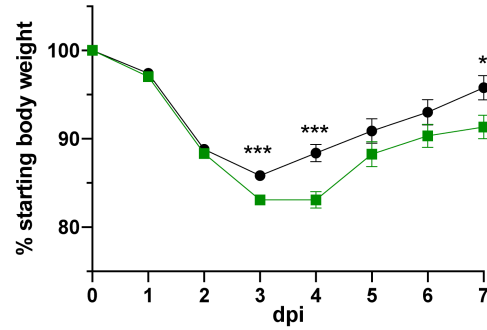
SARS-CoV-2 MA10
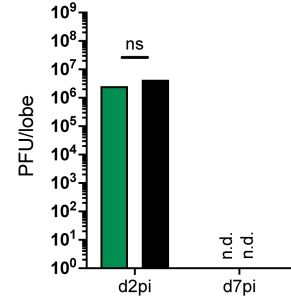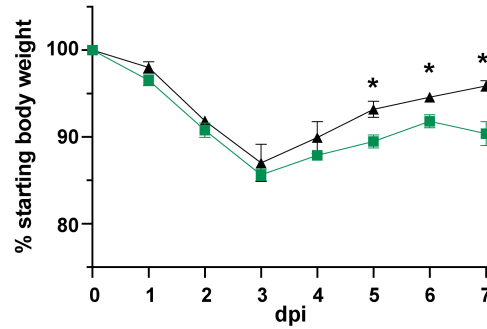
Figure 6
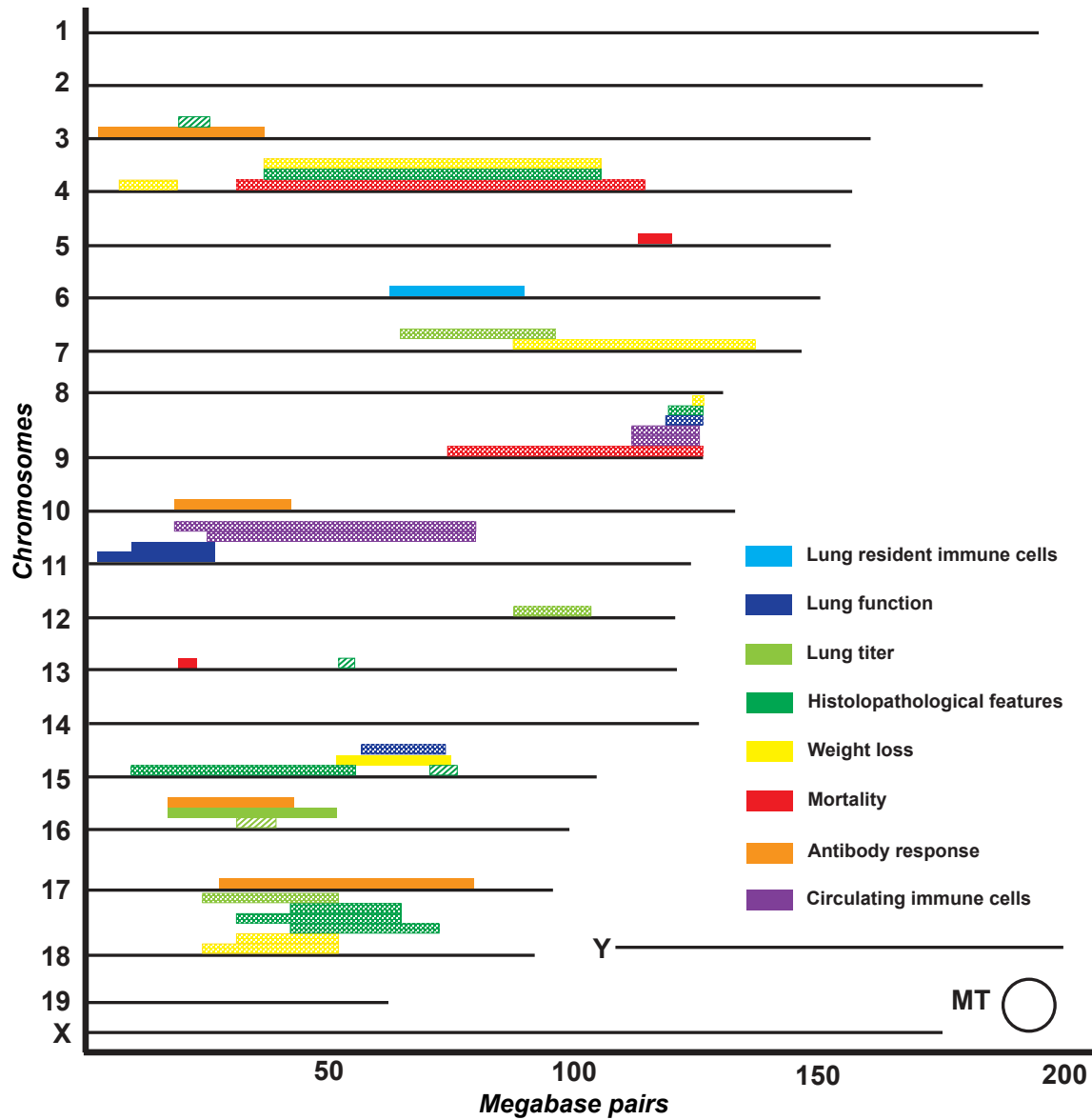
Table 1

QTL ID	Population	Chromosome [Mb]	Phenotype(s) (days post infection- dpi)	Haplotype(s)[+]	phenotypic variation [%]
Pre-CC					
*HrS*1	Pre-CC	chr3:18.3-26.8	Perivascular cuffing (4dpi)	BH/ACDEFG	26%
*HrS*2	Pre-CC	chr16:31.5-36.7	Viral titer (4dpi)	G/ABCDEFH	22%
*HrS*3	Pre-CC	chr15:72.2-76.0	Eosinophilia (4dpi)	A/BCDEFGH	26%
*HrS*4	Pre-CC	chr13:52.7-54.9	Perivascular cuffing (4dpi)	F/ABCDEGH	21%
CC-RIX					
HrS10	CC-RIX	chr13: 20.3- 23.7	HKU3-MA mortality	FG/ABCDEH	OR* 6.13
HrS11	CC-RIX	chr5: 112.9-118.8	HKU3-MA mortality	C/ABDEFGH	OR* 10.45
HrS12	CC-RIX	chr15: 51.5- 75.6	HKU3-MA weight loss (4dpi)	G/ABCDEFH	3.4%
HrS13	CC-RIX	chr16:18-51.1	SARS viral titer (2dpi)	C/G/ABDEFH	15.94%
HrS14	CC-RIX	chr11: 9.05- 28.66	PenH (2dpi)	D/CEH/ABFG	11.65%
HrS15	CC-RIX	chr11: 3.26- 28	Rpef (4dpi)	ABCEFGH/D	6.48%
HrS17	CC-RIX	chr17: 27.4- 78.3 chr17: 27.4- 78.3	IgG1 (N) (32dpi) Total IgG (N) (32dpi)	A/BCDEFH/G	19.97% 18.53%
HrS18	CC-RIX	chr16: 18.1- 43.8	Total IgG (N) (32dpi)	ABCDEFH/G	22.75%
HrS19	CC-RIX	chr10: 17.4- 130.5	Total IgG (N) (32dpi)	ABCDEH/FG	10.71%
HrS20	CC-RIX	chr3: 3.1- 35.4	Total IgG (N) (32dpi)	G/ABCDEFH	10.83%
HrS22	CC-RIX	chr6:67.2- 85	CD8^{+} DCs [%] (4dpi)	F/ABCDEGH	8.17%
CC011xCC074-F2					
HrS24	CC011xCC074-F2	chr4:32.95-114.54	Mortality	CC011: G,H,C CC074:A/H, A/D, D, E, F	OR* 4.34
HrS25	CC011xCC074-F2	chr4: 6.38-17.97	Weight loss in males (4dpi)	CC011: G, B CC074: A	12.57%
HrS26	CC011xCC074-F2	chr9:74.94-124.06 chr9:117.38-124.07 chr9:116.24-124.07	Mortality Hemorrhage (4dpi) PenH (2dpi)	CC011: B, G CC074: A	OR* 3.15 10.24% 7.76% 11.8%

		chr9:111.54-122.63	Periph. neutrophils (4dpi)		12.39%
		chr9:111.54-122.63	Periph. lymphocytes (4dpi)		
HrS27	CC011xCC074-F2	chr11:26.44-80.76 chr11:17.89-80.76	Periph. neutrophils (4dpi) periph. lymphocytes (4dpi)	CC011: H, B, H CC074: C	5.5% 5.6%
HrS28	CC011xCC074-F2	chr15:58.66-74.04	PenH (2dpi)	CC011: H CC074: B	8.48%
CC003xCC053-F2					
HrS5	CC003xCC053-F2	chr18:24.76-51.25 chr18:31.63-51.25 chr18:42.85-73.43 chr18:31.63-65.17 chr18:42.85-65.17 chr18:24.76-51.2 chr18:24.76-51.2	Weight loss (3dpi) Weight loss (4dpi) Hemorrhage (4dpi) Perivascular cuffing (4dpi) Edema (4dpi) Viral titer (4dpi)	CC003: A, G CC053: C/G, G, B, B/D, B/C, D	6%-13.2%
HrS6	CC003xCC053-F2	chr9:121.77-end	Weight loss (3dpi)	CC003: B, B/D CC053: H	7%
HrS7	CC003xCC053-F2	chr7:83.45-129.93 chr7:69.79-96.66	Weight loss (4dpi) Viral titer (4dpi)	CC003: B, C, B/C CC053: G/H, H, D	6.8% 14.4%
HrS8	CC003xCC053-F2	chr12:88.54-103.21	Viral titer (4dpi)	CC003: D CC053:F/H	4.27%
HrS9	CC003xCC053-F2	chr15:10.7-57.3	Hemorrhage (4dpi)	CC003: G, E/G, G CC053: D, C, F	9.4%
HrS23	CC003xCC053-F2	chr4:35.61-104.04 chr4:35.61-104.04	Hemorrhage (4dpi) Weigh loss (4dpi)	CC003: H, E, G, H CC053: F, G, F	6.86% 6.22%

*QTL influencing mortality calculate an Odds Ratio (OR) for disease rather than a % of variation explained. For both the CC-RIX and the CC-F2, Odds Ratios for specific loci are calculated with a full model of all mortality loci, to better estimate their independent effects.
+Haplotype effects are described for each QTL. For the Pre-CC and CC-RIX, the haplotypes are separated based on the allele effect splits between founder haplotypes (A=A/J, B=C57BL/6J, C=129S1/SvImJ, D=NOD/ShILtJ, E=NZO/HiLtJ, F=CAST/EiJ, G=PWK/PhJ, H=WSB/EiJ). In CC-F2 crosses, the haplotypes listed are those present in the given parent strains from the proximal to distal ends of each region
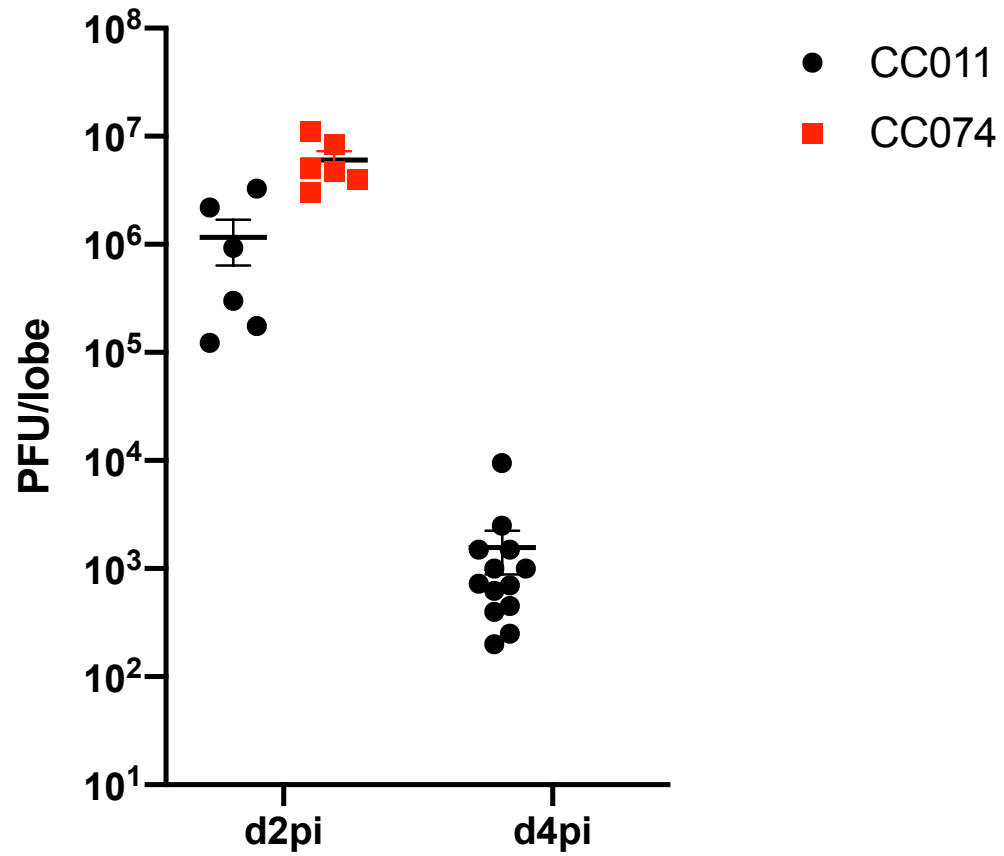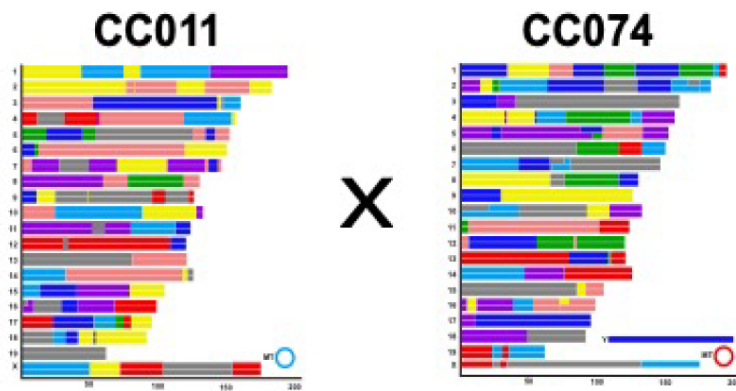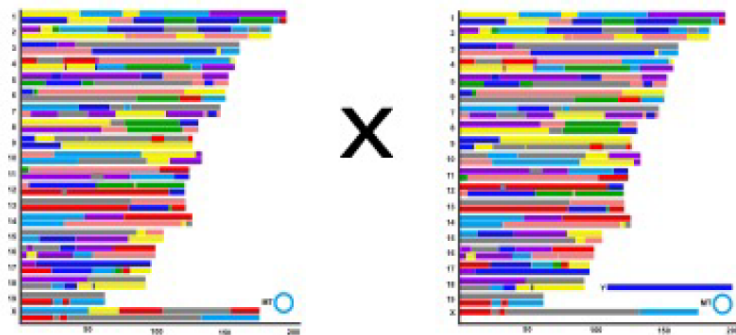
Figure S1

Figure S2

Figure S3

Figure S4

Figure S5

a.

Bronchoalveolar Lavage (BAL) Flow

Bronchoalveolar Lavage (BAL) Flow

b.

CCL2 · CCL5 · G-CSF · Eotaxin · IL17 · IL13

C57BL/6NJ
CCR9$^{-/-}$
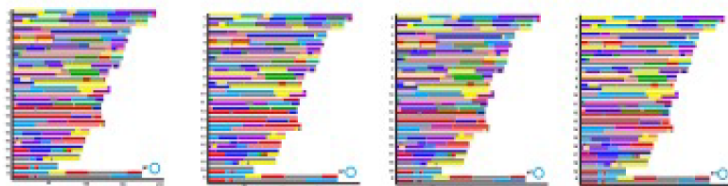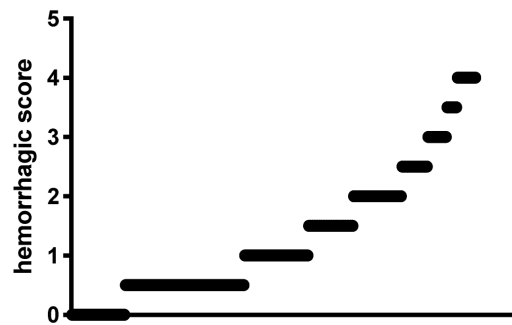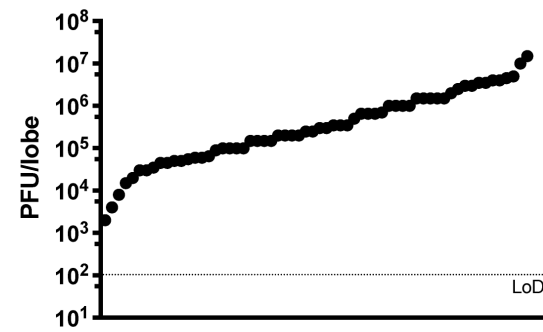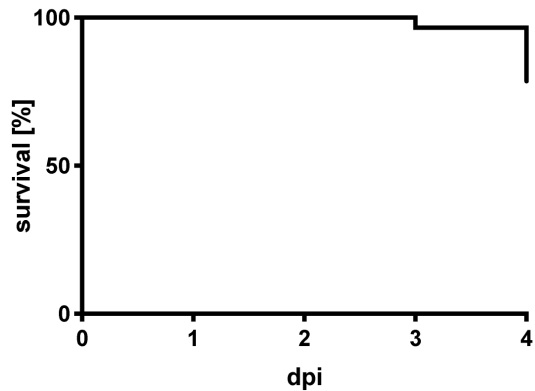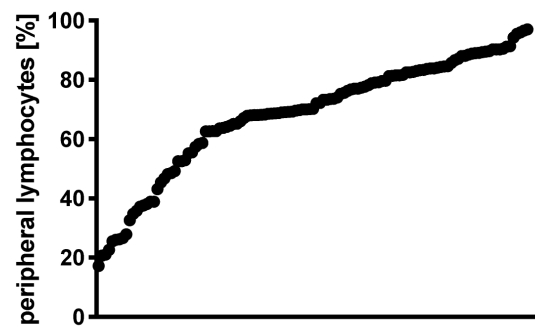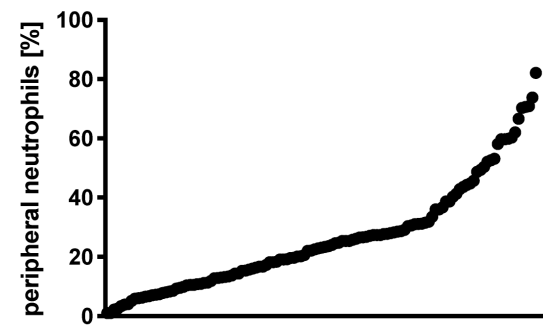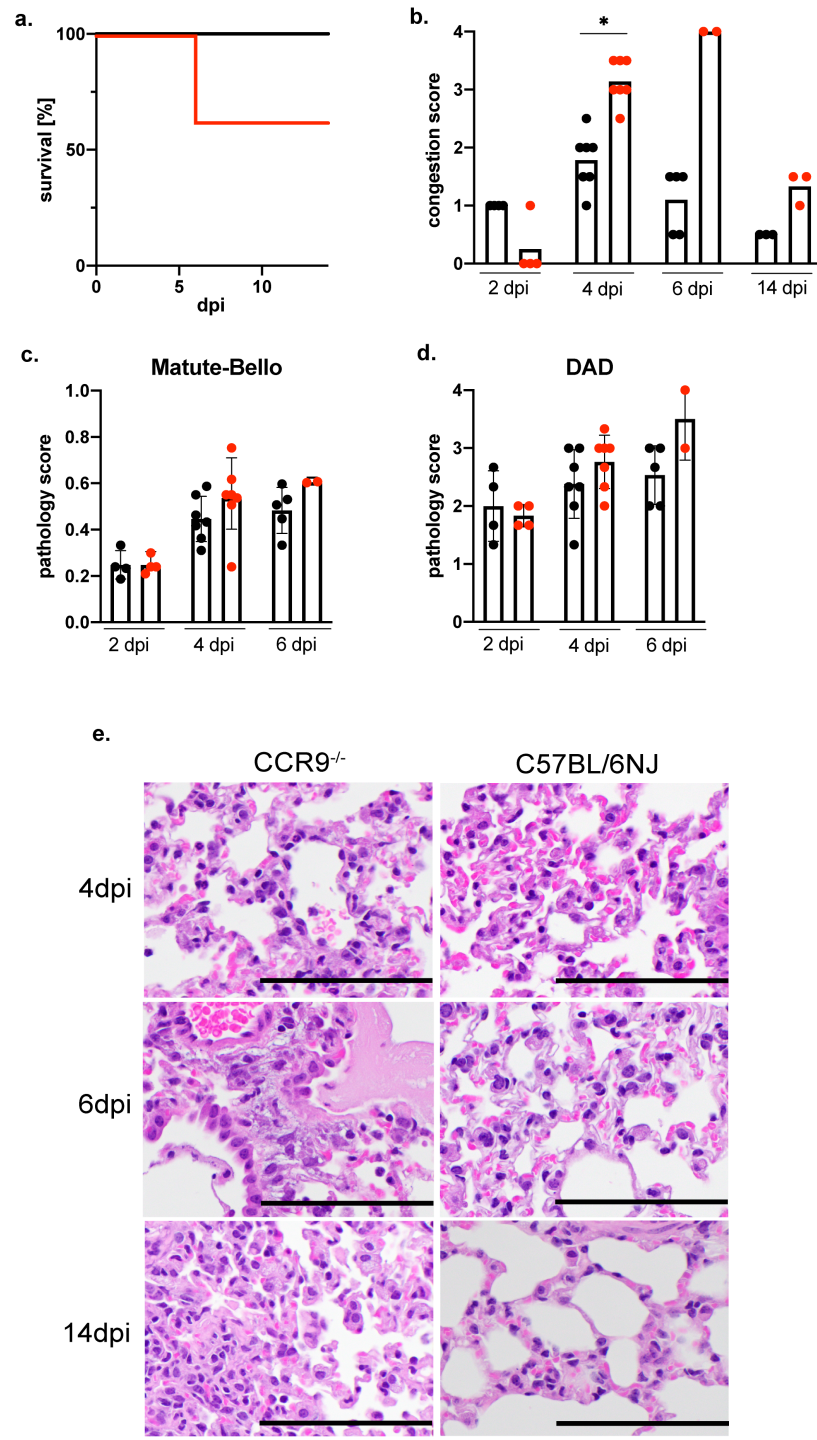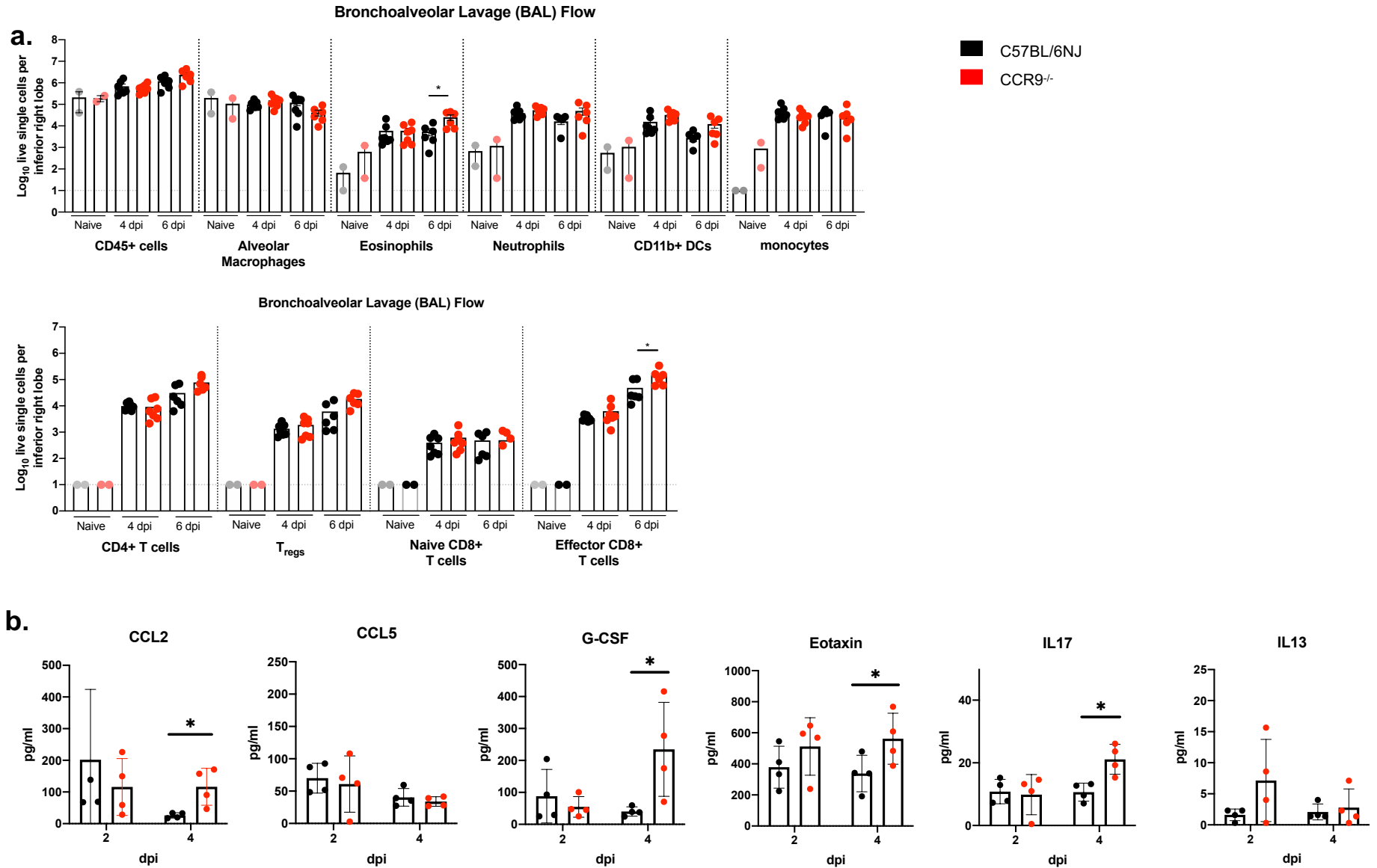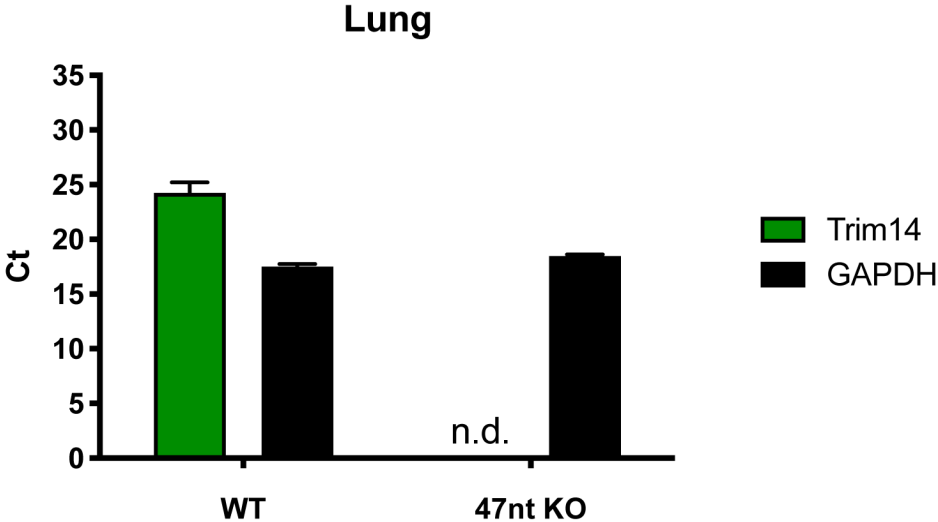
Figure S6

Figure S7
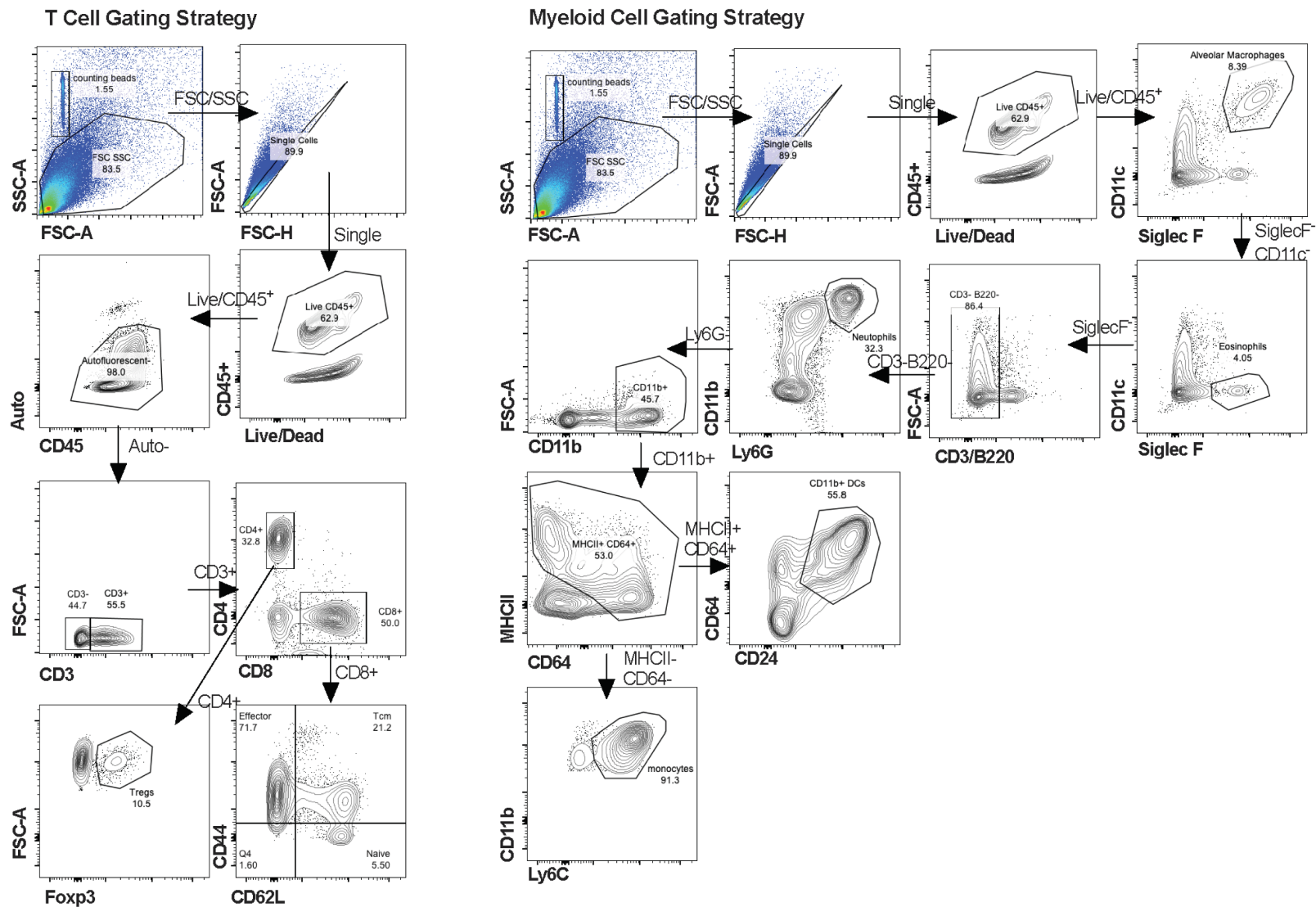
Table S1

QTL ID	Chromosome [Mb]	Phenotype(s) (days post infection – dpi)	Haplotype(s)[+]
CC011xCC074-F2 suggestive loci			
HrS29	chr3: 7.2-159.1	Mortality (4dpi) Hemorrhage (4dpi)	CC011: C, C/D, D, A, D, E CC074: D, H, B, B/F, B/D, B
HrS30	chr9: 28.2-124.1	Weight loss (4dpi) Mortality (4dpi) Weight loss females (4dpi)	CC011: B, G, B CC074: A
HrS31	chr13: 31.9-90.3	Hemorrhage (4dpi) Periph. monocytes (4dpi)	CC011: B, C CC074: G, D
HrS32	chr14: 33.8-114.8	PenH (2dpi)	CC011: C CC074: E, H, G
HrS33	chrX: 6.2- 93.9	Rpef (2dpi) Periph. neutrophils (2dpi)	CC011: E, C/E, E, A, G CC074: G, B
CC003xCC053-F2 suggestive loci			
HrS34	chr3: 58- 148.4	Weight loss (3dpi)	CC003: B, G, H, G CC053: C/D, C, D, A, E
HrS35	chr17: 6- 79	Weight loss (3dpi)	CC003: C/D, C, C/D, D, B CC053: G, E, G, H, A, G, H
HrS36	chr9: 3.6Mb-74.9Mb	Weight loss (4dpi), Titer (4dpi), Edema (4dpi)	CC003: C, B CC053: B, E
HrS37	chr10: 5.9Mb-86.3Mb	Titer (4dpi)	CC003: C, H CC053: H, B, A
HrS38	chrX: 9.4Mb-169.5Mb	Titer (4dpi)	CC003: C, G, C/G, C/E, C, E CC053: A, C, B, F
HrS39	chr2: 4.3Mb-181.8Mb	mortality (4dpi)	CC003: D, B, E CC053: B, E, G, E, A, C, F
HrS41	chr6: 34.2Mb-114Mb	Interstitial septum (4dpi), Airspace inflammation (dpi4), Eosinophils (4dpi)	CC003: B, E CC053: G, A, A/D, G
HrS42	chr11: 37Mb-121.6Mb	Edema (4dpi)	CC003: A/C, B/C, A/C, B/H, B, E, H, C, E CC053: B
[+]Haplotype effects are described for each QTL. For F2 crosses, the haplotypes listed are those present in the given parent strains from the proximal to distal ends of each region (A=A/J, B=C57BL/6J, C=129S1/SvImJ, D=NOD/ShILtJ, E=NZO/HiLtJ, F=CAST/EiJ, G=PWK/PhJ, H=WSB/EiJ). In			